A MEMS DUAL VERTICAL ELECTROMETER AND ELECTRIC FIELD-MILL

THESIS

George C. Underwood, Second Lieutenant, USAF

AFIT-ENG-MS-19-M-063

DEPARTMENT OF THE AIR FORCE
AIR UNIVERSITY

AIR FORCE INSTITUTE OF TECHNOLOGY

Wright-Patterson Air Force Base, Ohio

DISTRIBUTION STATEMENT A.
APPROVED FOR PUBLIC RELEASE; DISTRIBUTION UNLIMITED.

The views expressed in this thesis are those of the author and do not reflect the official policy or position of the United States Air Force, Department of Defense, or the United States Government. This material is declared a work of the U.S. Government and is not subject to copyright protection in the United States.

AFIT-ENG-MS-19-M-063

A MEMS DUAL VERTICAL ELECTROMETER AND ELECTRIC FIELD-MILL

THESIS

Presented to the Faculty

Department of Electrical and Computer Engineering

Graduate School of Engineering and Management

Air Force Institute of Technology

Air University

Air Education and Training Command

In Partial Fulfillment of the Requirements for the

Degree of Master of Science

George C. Underwood, B.S.E.E.

Second Lieutenant, USAF

March 2019

DISTRIBUTION STATEMENT A.
APPROVED FOR PUBLIC RELEASE; DISTRIBUTION UNLIMITED.

AFIT-ENG-MS-19-M-063

A MEMS DUAL VERTICAL ELECTROMETER AND ELECTRIC FIELD-MILL

THESIS

George C. Underwood, B.S.E.E.

Second Lieutenant, USAF

Committee Membership:

Maj. Tod V. Laurvick, PhD
Chair

Dr. Hengky Chandrahalim, PhD
Member

Dr. Frank Kenneth Hopkins, PhD
Member

AFIT-ENG-MS-19-M-063

Abstract

Presented is the first iteration of a Microelectromechanical System (MEMS) dual vertical electrometer and electric field-mill (EFM). The device uses a resonating structure as a variable capacitor that converts the presence of a charge or field into an electric signal. Previous MEMS electrometers are lateral electrometers with laterally spaced electrodes that resonate tangentially with respect to each other. Vertical electrometers, as the name suggests, have vertically spaced electrodes that resonate transversely with respect to each other. The non-tangential movement reduces damping in the system. Both types demonstrate comparable performance, but the vertical electrometer does so at a fraction of the size. In addition, vertical electrometers can efficiently operate as an electric field sensor. The electric field sensor simulations did not compare as well to other MEMS electric field sensors. However, the dual nature of this device makes it appealing. These devices can be used in missiles and satellites to monitor charge buildup in electronic components and the atmosphere [11]. Future iterations can improve these devices and give way to inexpensive, high-resolution electrostatic charge and field sensors.

Acknowledgments

I would first like to thank my advisor, Maj Laurvick for trusting me in this endeavor, for never having doubts even when I had many. I would also like to thank Dr. Chandrahalim for his constant support and vast knowledge in this subject, and Dr. Frank (Ken) Hopkins for his intellect and willingness to be on the committee. I also thank everyone in the MEMS Group for the fraternity that made the past year and a half so enjoyable. I appreciate Dr. David Torres for his friendship and assistance at AFRL. I would next like to thank my family. Mom and Dad, thank you for everything; you inspire me to challenge myself and not to live life with an excuse. I sincerely thank Blaine Underwood, my biggest competition and role model. You're the iron to my iron, we sharpen each other. Of course, I thank my beautiful Fiancée for being a beacon of joy in difficult times. Finally, I thank God, the guidance of the Holy Spirit, the immaculate heart of Mary, the protection of St. Joseph, and all the angels and saints for assisting me day-to-day.

George C. Underwood

Table of Contents

Page

Abstract iv
Table of Contents vi
List of Figures ix
List of Tables xiii
I. Introduction 1
II. Literature Review 4
2.1 Chapter Overview 4
2.2 Variable Capacitor Based MEMS Electrostatic Charge and Field Sensors 4
2.3 Noise Analysis 5
2.3.1 Thermal Noise 7
2.3.2 Leakage 8
2.3.3 Flicker Noise 10
2.3.4 KT/C Noise 11
2.3.5 Brownian Noise 12
2.3.6 Noise Mixing 13
2.3.7 Feedthrough 14
2.4 Riehl's Electrometer 18
2.5 Riehl's E-field Sensor 20
2.6 Mechanics 21
2.6.1 Actuation 22
2.6.2 Suspension 26
2.6.3 Damping 27

2.7 Conclusion........28

III. Theory and Methodology........32

3.1 Chapter Overview........32

3.2 Fabrication........33

3.3 Electromechanical Characterization........35

3.4 Electrometer Sensitivity Analysis........38

3.5 Electrometer Noise Analysis........41

3.6 Experimental Setup of Electrometer........43

3.7 Electric Field-Mill Sensitivity Analysis........45

3.8 Electrostatic Field-Mill Noise Analysis........47

3.9 Experimental setup of EFM........49

3.10 Summary........50

IV. Results........51

4.1 Chapter Overview........51

4.2 Simulation Results........51

4.2.1 Mechanical Simulations........51

4.2.2 Electrometer Simulations........53

4.2.3 E-Field Simulations........54

4.3 Electromechanical Results........57

4.3.1 Mechanical Measurements........58

4.4 Electrometer Results........62

4.5 Electric Field Sensor Results........62

4.6 Conclusion........63

V. Analysis 64
5.1 Chapter Overview 64
5.2 Mechanical Results Analysis 64
5.2.1 Resonant Frequency 64
5.2.2 Effects of Defects 65
5.2.3 Mechanical Voltage Signal at Resonance Compared to Simulations 67
5.3 Electrometer Results Analysis 69
5.3.1 Simulated Electrometer Charge Conversion Gain 69
5.3.2 Electrometer Theory Compared to Simulations 70
5.4 EFM Results Analysis 74
5.4.1 Simulated EFM Responsivity 74
5.4.2 EFM Theory Compared to Simulations 75
5.5 Chapter Summary 76
VI. Conclusion and Recommendations 77
6.1 Chapter Overview 77
6.2 Conclusion 77
6.2.1 Electrometer 77
6.2.2 EFM 79
6.3 Recommendations 80
6.4 Future Work 83
6.5 Chapter Summary 85
Appendix 86
Bibliography 87

List of Figures

Figure Page

1. Block diagram of a basic electrometer. 6
2. Block diagram of a basic electrometer in coulometer mode. 7
3. Noise representation of a FET transistor. 8
4. A linear model of electrometer input leakage. 9
5. A conceptual plot of input-referred spectral-noise of a transistor as a function of frequency. 11
6. Example noise model of a feedback system. 13
7. Open loop voltage amplifier. 14
8. Feedthrough voltage circuit. 15
9. Feed through voltage circuit with differential sensing. 16
10. Feed through voltage circuit with differential sensing and driving. 17
11. Top view of a simple schematic of a MEMS electrometer. 19
12. A depiction of Vertically spaced electrodes (a), and laterally spaced electrodes (b). 21
13. (a) shows a typical differentially actuated comb drive resonator. (b) shows an equivalent mass-spring-damper system of (a). 23
14. Folded-flexure suspensions: (a) Basic double-folded-flexure suspension, (b) Split dual folded-flexure suspension. 26
15. Depictions of squeeze film damping (a) and slide film damping (b). 28
16. (a) shows a simple 3D model of the dual sensor design. (b) shows the cross section of (a). 32
17. A cross section view showing all seven layers of the PolyMUMPs Process. 33

18. Experimental setup for mechanical characterization. 37

19. This figure shows conceptual pictures of the variable capacitor. (a) shows a simplified circuit where Cp is the lumped up parasitic capacitances, Cv is the variable capacitor, and Q is the charge that induces the sense voltage Vi. (b) is a block diagram of the same circuit. (c) is a 2D model of one electrode. (d) is a 3D model of (c). 39

20. Noise model of the Electrometer. 42

21. Experimental Setup for testing the electrometer mode. 44

22. Cross section of the shutter and sense electrodes while in EFS mode. 45

23. Noise model of EFS. 47

24. Electrical setup for testing the EFM. 49

25. Image of the device under test. 52

26. The primary mode of the DOT with a resonant frequency of 16.5 kHz. 52

27. (a) shows the structure created in COMSOL for the simulation with zero displacement. (b) shows the same structure that was displaced 4 microns. (c) shows the time depended capacitance between the electrode indicated by the arrow and the red electrodes. Warm colors represent areas with higher voltage and cool colors lower voltage. 54

28. The simulated capacitance between one sense finger and an e-field emitting source electrode. 55

29. Expected capacitance value for simulation. 56

30. The result of the COMSOL simulation showing electrostatic field lines emitting from the source electrode. 56

31. (a) is a 3D microscope image of the device showing unlevel top electrodes and (b) is a 2d cross section of (a). 57
32. SEM image of the beam suspension. 58
33. Frequency response measurement setup. 59
34. The frequency response of the resonator. (a) shows the RMS voltage measured by the lock-in amplifier with respect to frequency (with a gain of 500 thousand). (b) shows the same response normalized to an amplitude of 1. 60
35. Illustration of defects. 65
36. (a) shows the time domain capacitance between one top electrode and one bottom. (b) shows the capacitance in the frequency domain. Results are show for both the ideal electrode and deformed. 66
37. (a) shows the time domain capacitance between one bottom electrode and a source electrode 600 microns away. (b) shows the capacitance in the frequency domain. Results are shown for both the ideal electrode and deformed. 67
38. This figure shows the amplitude spectrum of the simulated voltage signal at resonance. A voltage of 2.5 V chosen as the sense voltage. 68
39. The figure above shows the amplitude spectrum of the simulated electrometer responsivity. 70
40. Solution to the integral in Equation (76) with respect to the alpha value. 73
41. The figure above gives the simulated results for responsivity of the EFM mode. 75
42. A depiction of a side contact vs. a center one. The side contact is less likely to form a connection with the edge of the chip. 81
43. A depiction of having dimples vs. no dimples. 81

44. An SEM image showing stiction of the device.. 81

45. SEM image of pillar used for preventing out of plane motion. 82

46. The figure shows the path of displacement for the grounded electrode in a fringe capacitor.. 83

List of Tables

Table Page

1. Review of MEMS Electrometers 30

2. Review of MEMS Electric Field Sensors 31

3. Design Parameters of Electrometer/EFM 35

4. Mechanical Values 61

5. Alias Structure for Factorial Analysis of Electrometer Responsivity Prediction 71

6. 2^4 Factorial Analysis for Electrometer Responsivity Prediction 72

7. 2^2 Factorial Analysis for EFM Responsivity Prediction 76

A MEMS DUAL VERTICAL ELECTROMETER AND ELECTRIC FIELD-MILL

I. Introduction

Microelectromechanical systems (MEMS) show potential for creating extremely sensitive charge sensors. These sensors, or electrometers, are used in mass spectrometry, for the detection of bio-analyte and aerosol particles, for the measurement of ionization radiation, in space exploration, in quantum computing, and in scanning tunneling microscopy[1]–[3]. Commercially, electrometers can sense a minimum equivalent charge of 5000 electrons [4]. MEMS electrometers have demonstrated detection of 6 electrons at room temperature and atmospheric pressure [3], [5], [6]. Other technologies have been used to detect charges smaller than one electron such as the single electron tunneling transistor. One such transistor resolved an equivalent charge of 1.9×10^{-6} electrons [1]. However, the sensing temperature was 4.2 Kelvin, which is too low for nearly all practical applications.

There exists a demand for more sensitive, more accurate charge detection at room temperature. For example, electrometers are used to measure the charge on large particles such as viruses. With the capability of detecting 15 electrons, these charge-detection electrometers could be used for DNA analysis [2]. Moreover, gas-detector electrometers could be used for car exhaust monitoring with a 500-electron resolution [4]. These applications cannot be realized with present commercial electrometers. MEMS

electrometers can provide an inexpensive solution to these applications. They are smaller than commercial electrometers and can be mass produced, they are made with inexpensive materials such as silicon, and they can be implemented with microelectronics more easily.

Previously reported MEMS electrometers are variable capacitors that convert a presence of a charge into an electric signal [2]–[4], [7]–[9]. The amplitude of the signal is linearly proportional to the charge. The use of mechanical variable capacitance is used in several sensing applications including pressure sensors, gyroscopes, accelerometers, and Electric field-mills (EFMs).

EFMs are the most prevalent devices used for quantifying electric fields today. They are superior to solid state sensors because of their long-term stability. They are used in weather applications for measuring atmospheric electric fields [10]. They are also used in the aviation industry to monitor electro-static build-up in missiles and satellites and thus prevent discharge [11]. EFMs can also be used as a non-contacting electrostatic voltmeter (ESV) given the correct feedback control [2]. EFMs detect electric fields by creating a variable capacitance between the source and the detector. However, EFM applications are limited by their size, power consumption, and relatively high cost [11]. MEMS can be a solution to all of these technology needs.

In general, there are two types of MEMS EFMs (as demonstrated by Riehl *et al.* [2]), ones that are made of vertically spaced electrodes and those that are made of laterally spaced electrodes. The difference between the two is discussed in Section 2.5. The main advantage of the vertically spaced EFM to the laterally spaced devices is that they create a less damped system. Less damping leads to less power needed in the system, which can lead to smaller feed-through voltage noise and more sensitive sensors.

MEMS electrometers, on the other hand, have only been demonstrated with laterally spaced electrodes. These devices suffer from high damping due to squeeze-film damping (Section 2.6.3). However, vertically spaced electrometers can reduce damping effects.

This work develops a theoretical model for the charge response of a vertically spaced MEMS electrometer. Physical devices were fabricated using the PolyMUMPs foundry process. They serve as a proof of concept behind the theory. Their ability to measure electric fields was also characterized. Uniquely, nonlinearities were created in the device to modulate the electric field signal to the second harmonic of the actuation voltage. The next chapter reviews important concepts for designing MEMS electrostatic charge and field sensors.

II. Literature Review

2.1 Chapter Overview

This chapter introduces essential concepts for the design of electrometers and electric field sensors. Noise is a limiting factor for any sensitive sensor. For example, to detect 1μV with a voltmeter, the noise floor would need to be smaller than 1μV. Any signal below the noise floor cannot be distinguished from the noise. MEMS resonators have been used to make extremely sensitive electrometers and electric field sensors. Riehl et al. developed the first MEMS electrometer in 2003 [2], [7]. This chapter presents the detection methods and fundamental theories of his electrometers and electric field sensors, as this research is mostly based off of his work. Then, discussed are important mechanical concepts for MEMS resonators. Finally, limitations and improvements of previous MEMS electrometers and electric field sensors are discussed.

2.2 Variable Capacitor Based MEMS Electrostatic Charge and Field Sensors

In 1785, Charles Coulomb reported that electrostatic charges exert a force on each other using a torsion balance, which he invented [4]. What he created was the first instrument that could quantify charge. In the early twentieth century, Millikan quantified the charge of a single electron by using an oil drop experiment [1]. In that experiment, he charged an oil drop and measured how strong an applied electric field had to be to prevent it from falling. By doing this several times with oil droplets of different charges, he was able to quantify the charge of a single electron. It wasn't until 1932 that Ross Gunn, at the Naval Research Laboratory, invented the first variable capacitor electrometer, known as a vibrating reed electrometer [4]. The variable capacitance was created by semicylindrical

electrodes, two stationary ones and two on a rotating shaft. Gunn was able to quantify a minimum charge of 4 fC (24,000 electrons) using this system. Since his invention, variable capacitance was the most common method used for measuring charge until the emergence of solid-state sensors. However, in more recent years, researchers demonstrated low cost, high-resolution MEMS electrometers [1]. The first MEMS electrometer was created by Riehl *et al.* [2], [7]. Their electrometer is discussed in more detail in Section 2.4.

Riehl *et al.* also demonstrated a MEMS electric field-mill (EFM) [2]. EFMs are superior to solid state sensors because of their long-term stability. EFMs can also be used as a non-contacting electrostatic voltmeter (ESV) given the correct feedback control [2]. ESVs measure potential by creating a variable capacitance between the source voltage and the detector. Loconto developed the first known MEMS EFM/ESV in 1993 [4]. He demonstrated a resolution of 10 mV at an electrode distance of 6 μm. Sections 2.4 and 2.5 describe, in more detail, the electrometer and EFMs developed by Riehl *et al.* Before reviewing these devices, the different noise sources in electrometer and EFM systems need to be understood.

2.3 Noise Analysis

There is some disagreement in literature on the exact definition of an electrometer [4]. This research follows the definition used by Keithley Instruments, a leading manufacturer of dc-electrical-measurement systems. Their definition of an electrometer is an instrument that incorporates all of the multimeter functions plus a coulometer mode and is characterized by high input impedance and high resolution [4]. The multimeter functions are voltage, current and resistance measurements. A coulometer measures charge. The

instrument developed in this research may be more accurately described as a coulometer with an EFM mode since it is only analyzed for measuring charge and electric field. However, the device can be used for the other electrometer functions.

A block diagram of an electrometer is shown in I.Figure 1. It consists of a shunt resistor followed by a fixed gain stage. Typically, R_i is very large (> 1 GΩ). The high impeadance allows for a large IR voltage drop across the resistor which is practical for low current measurements, such as measuring charge, large resistances, or voltages from a high source impedance [4].

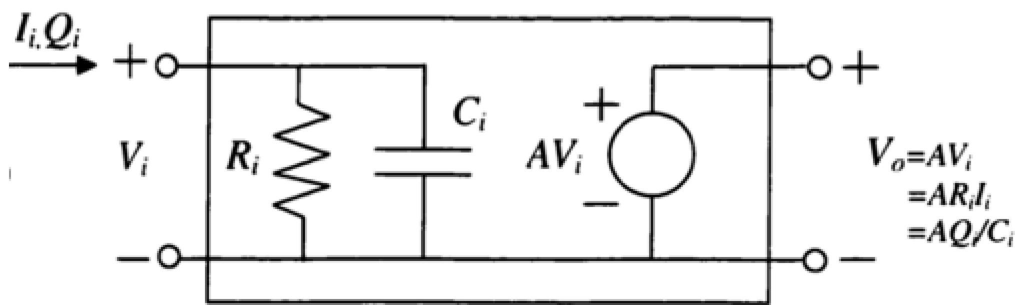

Figure 1. A block diagram of a basic electrometer (borrowed from [4]).

To measure charge, the input resistance should be as high as possible to allow the capacitor C_i to hold a charge long enough to make a measurement. An electrometer in coulometer mode can be represented by replacing R_i with an open switch as shown in Figure 2. It should be noted that the circuit in Figure 2 is the basis of the electrometer in this research. The switch is used to ground the input node. Still, with an open switch, there is some leakage current across the capacitor. The leakage current creates a sensitivity limit for the charge sensor as well as a source of noise. However, before reviewing limitations due to leakage current, thermal noise needs to be considered as well.

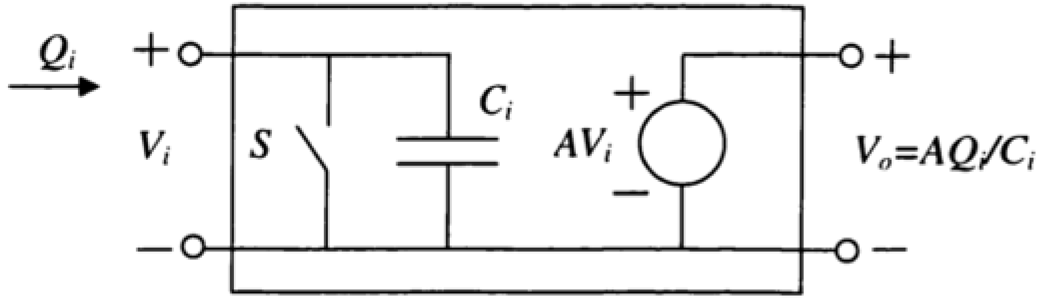

Figure 2. Block diagram of a basic electrometer in coulometer mode (borrowed from [4]).

2.3.1 Thermal Noise

Random thermal motion of electrons create noise in electronic circuits. The thermal voltage and current noise of a resistor with a resistance value of R are listed below [4]:

$$\bar{v}_n^2 = 4kTR\Delta f \tag{1}$$

$$\bar{i}_n^2 = \frac{4kT\Delta f}{R}. \tag{2}$$

These expressions are represented as the variance of the noise where k is Boltzmann's constant T is absolute temperature, and Δf is the bandwidth of the measurement. Typically, noise is represented by the variance divided by the bandwidth as shown in Equations (3) and (4):

$$\frac{\bar{v}_n^2}{\Delta f} = 4kTR \tag{3}$$

$$\frac{\bar{i}_n^2}{\Delta f} = \frac{4kT}{R}. \tag{4}$$

These representations are known as the spectral densities and are constant for white noise voltages [4]. Noise is also commonly represented as the square root of Equations (3) and (4). Therefore, noise is referred as some quantity per root Hertz (e.g. $\frac{nV}{\sqrt{Hz}}$).

The thermal noise of a field-effect transistor (FET) can be represented as a voltage-noise source (v_n) and a current-noise source (i_n) at the input of the device (Figure 3). The thermal noise spectral densities of the FET are [4]:

$$\frac{\bar{v}_n^2}{\Delta f} = 4kT\frac{2}{3g_m} \tag{5}$$

$$\frac{\bar{\imath}_n^2}{\Delta f} = 2qI_g + 4kT\frac{2}{3g_m}(2\pi f)^2 C_{gs}^2 \tag{6}$$

where g_m is the transconductance of the FET, C_{gs} is the gate-to-source capacitance, and I_g is the gate current. The current-noise spectral density contains two terms. The first, $2qI_g$, is the shot noise in the gate current of the FET. The second term is the input-referred thermal noise in the transistor channel [4].

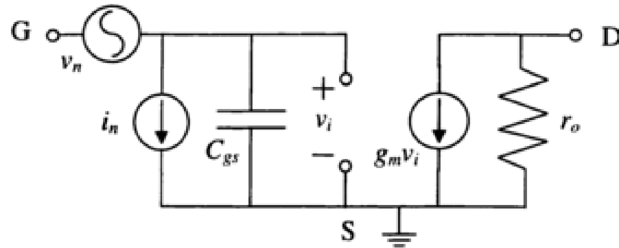

Figure 3. Noise representation of an FET transistor (borrowed from [4]).

2.3.2 Leakage

As mentioned before, a charge sensor ideally has an infinitely high input impedance so that charge can be held indefinitely on a capacitor. This gives an infinite amount of time to make a measurement and results in a high-resolution device. However, even with an open switch, a leakage current will be present across the capacitor.

Consider the input node of an electrometer shown in Figure 4. The leakage current is represented by the DC current source I_l with a leakage resistance R_l. The equilibrium

voltage of this circuit is $v_{eq} = R_l I_l$. If this voltage exceeds the input range of the initial amplifier stage, the circuit cannot be operated without a switch [4]. The equilibrium voltage also creates an equilibrium charge equal to $Q_{eq} = R_l I_l C_i$. Measuring charges much smaller than this is an extremely difficult task. For instance, to measure one electron from an equilibrium charge of one million electrons, measurement instruments would need to resolve one part per million in voltage. Also, the time required to make a measurement is limited by the time constant $\tau = RC$ [4].

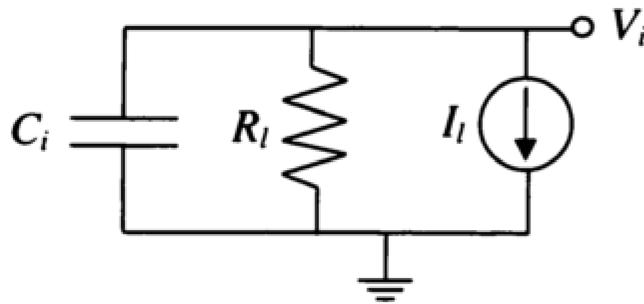

Figure 4. A linear model of electrometer input leakage (borrowed from [4]).

If a switch is used to set the input charge to zero, then the equilibrium voltage is of no concern [4]. However, leakage current will build up a charge over time. If the leakage current is comparable to the charge to be measured divided by the time to measure it, this presents a resolution limit [4].

In addition to creating measurement limitations for electrometers, leakage current paths also introduce noise to the system. Thermal noise from resistors and shot noise from other components inject charge noise onto the input of the electrometer [4]. Equation (1) gives the thermal noise of a resistor. The shot noise is represented by

$$\frac{\bar{\iota}_{sn}^2}{\Delta f} = 2qI_t \tag{7}$$

where I_t is the DC current creating the shot noise [4]. If the leakage time constant is much smaller than the time taken to make a measurement, then the worst-case scenario can be made that all of the leakage current noise is integrated to the input capacitor of the electrometer [4]. The resultant charge noise is

$$\bar{Q}_{sn} = \frac{1}{2\pi\sqrt{f_s}}\sqrt{\frac{\bar{\iota}_{sn}{}^2}{\Delta f}} \tag{8}$$

where f_s is the sampling frequency [4]. The expression in Equation (8) assumes that one is only interested in the difference between two consecutive samples. If one is interested in the absolute charge noise, then it is assumed that the shot noise comes into equilibrium with the input resistance [4]. The resultant RMS noise is

$$\bar{Q}_{sn} = R_l C_i \bar{\iota}_{sn} = \sqrt{\frac{1}{2} q I_l R_l C_i}. \tag{9}$$

Minimizing R_l and I_l is crucial for making highly sensitive charge sensors. This can be done by surrounding the input of the device with a good insulator such as silicon dioxide or silicon nitride [4].

2.3.3 Flicker Noise

Flicker noise, or 1/f noise, is a dominant noise source in low-frequency circuits [4]. All transistors have some 1/f noise. The 1/f noise of a FET can be modeled using the same noise model in Figure 3. Equations (10) and (11) give the spectral noise densities of the circuit:

$$\frac{\bar{v}_{nf}^2}{\Delta f} = \frac{K_f}{WLC_{ox}f} \tag{10}$$

$$\frac{\bar{\iota}_{nf}^2}{\Delta f} = \frac{4\pi^2 C_{gs}^2 K I_D^a f}{g_m^2}. \tag{11}$$

W and *L* are the width and length of the transistor channel, I_D is the drain current, and C_{gs} is the gate-to-source capacitance. K_t, K, and a depend on the fabrication process for the FET. The 1/f noise takes the shape of the frequency dependent signal shown in Figure 5. The frequency at which the l/f and thermal-noise sources are equal is called the 1/f noise corner. Measuring the signal at a higher frequency than the noise corner frequency significantly reduces noise effects.

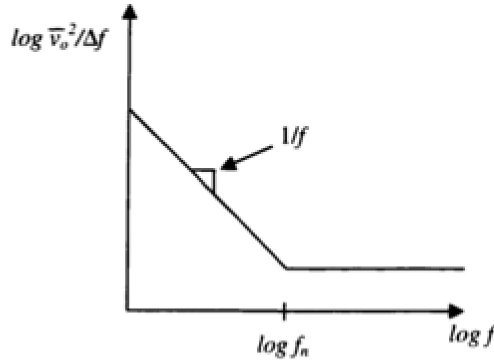

Figure 5. A conceptual plot of input-referred spectral-noise of a transistor as a function of frequency. f_n represents the 1/f noise corner of the transistor (borrowed from [4]).

2.3.4 KT/C Noise

Capacitors create no thermal noise, which is why they are often used in low-noise circuits [4]. However, purely capacitive circuits build up charge over time and create large voltage drops [4]. Usually a switch is used to bias the voltage back to zero. Adding a switch

(as in the coulometer in Figure 2) creates thermal noise from the on resistance of the switch. This thermal noise is called KT/C noise [4].

The voltage-noise variance of the on-resistance is given in Equation (1). When the switch is opened, some of the voltage-noise will still be present on the capacitor and has a variance of

$$\bar{V}_n^{\ 2} = \frac{kT}{C}. \tag{12}$$

In an electrometer, we are interested in the residual charge built up on the capacitor from the voltage noise. The variance of the residual charge is given by [4]

$$\bar{Q}_n^{\ 2} = kTC. \tag{13}$$

2.3.5 Brownian Noise

The mechanical equivalent of thermal noise is Brownian noise. Random thermal motion creates a displacement variance in mechanical elements [4]. This random motion is prevalent in high-resolution displacement sensors, such as accelerometers, and sets a lower bound for detection [4]. The spectral density of displacement-noise in a lumped spring-mass-damper system at resonance is given by [4]

$$\frac{\bar{x}_n^{\ 2}}{\Delta f} = \frac{kT}{\pi^2 f^2 b} \tag{14}$$

where *b* is the damping coefficient.

This research utilizes suspended vibrating mass structures to modulate electrical signals. The peak amplitude vibration is in the order of micrometers. The Brownian noise in this system is in the order of pico-meters and does not create a significant resolution limit [4].

2.3.6 Noise Mixing

The device in this research contains a time varying capacitor. For any circuit with time varying components, the way in which noise is modulated needs to be considered [4]. Noise mixing is present in voltage amplifier feedback circuits as shown in Figure 6 [4].

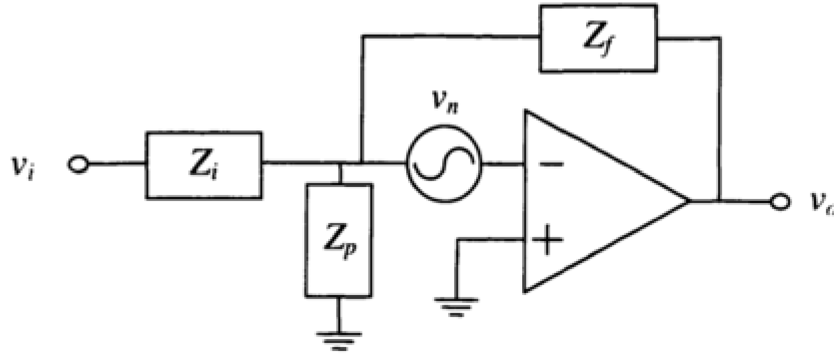

Figure 6. Example noise model of a feedback system (borrowed from [4]).

The amplifier amplifies the input voltage, v_i, to the output voltage, v_0. The circuit contains three impedance sources: Z_i the input impedance, Z_p the parasitic impedance, and Z_f the impedance of the feedback path. The amplifier also contains a generic noise generator v_n. The gain of the circuit is

$$\frac{v_0}{v_i} = \frac{Z_f}{Z_i}. \tag{15}$$

If either Z_f or Z_i varies at a frequency f_0, then a DC input voltage will generate a component of the output voltage at f_0. Also, the noise voltage will create a component of v_0 at the same frequency. The response of the circuit to the amplifier noise is referred as the noise transfer function (NTF) and is given by [4]

$$NTF = \frac{v_0}{v_n} = \frac{Z_f + Z_i||Z_p}{Z_i||Z_p}. \tag{16}$$

If the signal is analyzed at the modulation frequency, then the way 1/f noise is up-mixed to the detection frequency needs to be considered. All feedback circuits suffer from 1/f noise.

However, consider the open loop voltage amplifier shown in Figure 7. The gain of the circuit is given by [4]

$$\frac{v_0}{v_i} = A\frac{Z_p}{Z_i + Z_p}. \tag{17}$$

Any variation in Zi will create a component of v_0 at the frequency of the variation. However, the NTF of the circuit is simply A [4]. So, no low frequency noise is up-mixed to the modulation frequency.

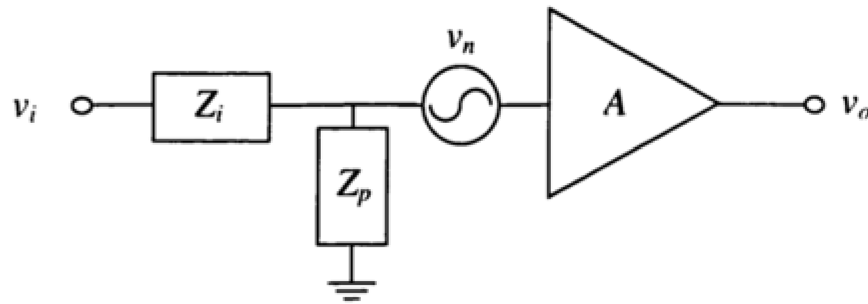

Figure 7. Open loop voltage amplifier (borrowed from [4]).

2.3.7 Feedthrough

For many MEMS applications, structures need to be actuated by electrical signals. The actuation signal can be coupled to the sense node of the instrument through parasitic capacitances. This coupling is unwanted because it interferes with the signal to be detected. This type of interference is known as feedthrough.

As an example, consider the generic sensing circuit of Figure 2.8. Here, v_d is the AC drive signal used to actuate the sensor, typically on the order of 1 V_{pp} [4]. v_s is the signal to be sensed, C_x is the feedthrough capacitance, and C_s is the sense capacitance.

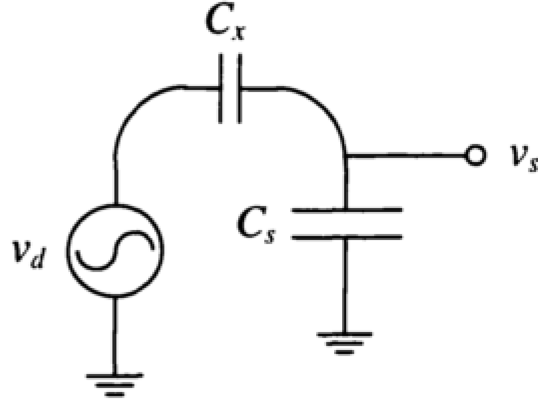

Figure 8. Feedthrough voltage circuit (borrowed from [4]).

The feed-through voltage at the sense node, v_s, is equal to the capacitor-voltage-divider equation [4]:

$$v_f = v_d \frac{C_x}{C_s + C_x}. \tag{18}$$

Typical values for C_s are in pico-farads, and C_x in femto-farads [4]. These values would yield a feedthrough signal of 1 mV_{pp}, which would be catastrophic on the performance of the sensor.

The feedthrough voltage can be reduced by differential sensing. Consider the circuit in Figure 9. Here, we assume that the signal to be measured is on v_{s+} and v_{s-} is used as a reference, or that the two nodes are equal and opposite in voltage. In this case, the value of interest is the difference between the two nodes. This would result in a feedthrough signal equal to [4]

$$v_f = v_d \frac{C_{x+}}{C_{s+} + C_{x+}} - v_d \frac{C_{x-}}{C_{s-} + C_{x-}}. \tag{19}$$

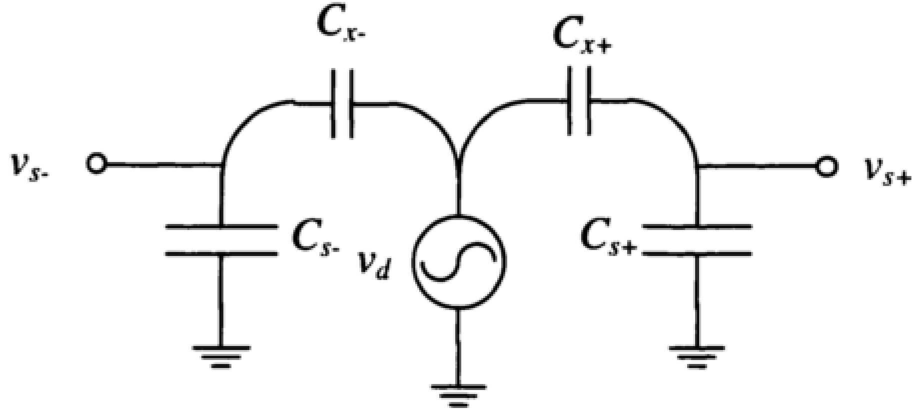

Figure 9. Feed through voltage circuit with differential sensing (borrowed from [4]).

We can typically assume that C_s is much larger than C_x, and that C_{s+} and C_{s-} are well matched. If the mismatch between the two feedthrough capacitors are expressed as

$$C_{s-} = C_{s+}(1 + \delta_1) \tag{20}$$

then the feedthrough signal can be written as [4]

$$|v_f| = |v_d| \frac{|\delta_1| C_x}{C_s}. \tag{21}$$

The feedthrough signal can be further reduced by implementing differential actuation [4]. This refers to actuating a mechanical structure with equal and opposite waveforms, one on each side. Adding differential actuation to differential sensing results in the circuit shown in Figure 10. The resultant feedthrough signal is further reduced to

$$|v_f| = |v_d| \frac{C_x}{C_s} |\delta_1||\delta_2| \tag{22}$$

where δ_2 is the mismatch between the upper and lower feedthrough capacitances [4]. If all of the feedthrough capacitances match within 1%, then the original 1 mV signal will be reduced to 100 nV.

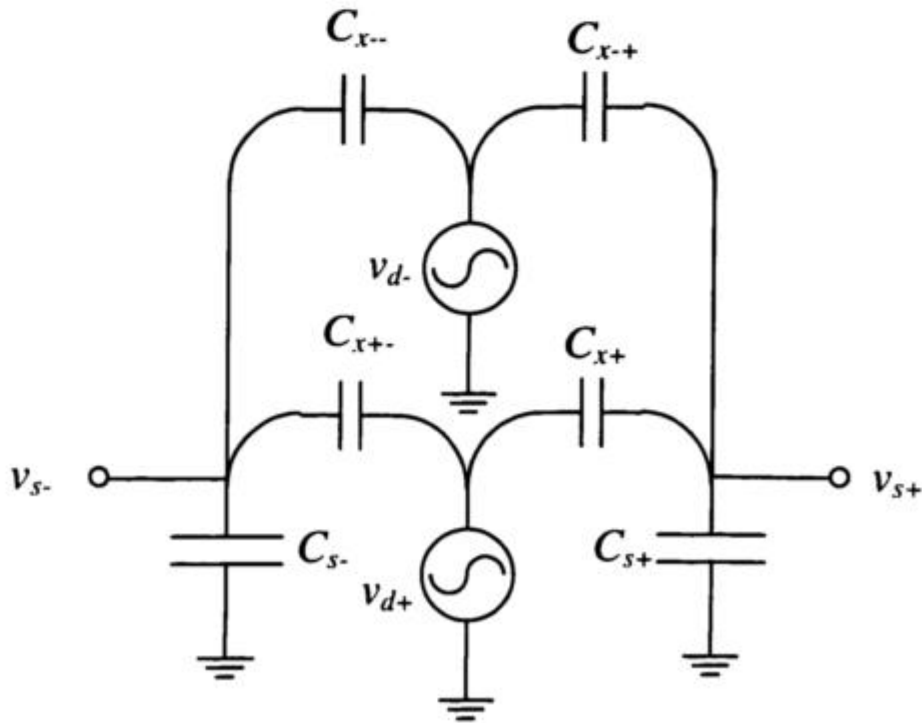

Figure 10. Feed through voltage circuit with differential sensing and driving (borrowed from [4]).

Still, another technique can be implemented to reduce feedthrough by separating the drive signal from the sense signal in frequency or phase. It is often advantageous to create nonlinearities in an electrical, mechanical system so that the signal is generated at a harmonic of the drive frequency [4]. This is referred to as harmonic sensing. A narrow band detector can amplify the signal at the harmonic of the drive frequency, completely filtering out the feedthrough [4]. However, in real-world systems, some of the drive signal is distorted and appears at the harmonic frequency. Let's say we drive a system with an AC voltage, v_d, at a frequency f, and we detect the signal at $2f$. The distortion would be defined as [4]

$$HD_2 = \frac{|\hat{v}_d(2f)|}{|\hat{v}_d(f)|}. \tag{23}$$

If this method is added to the two previous, the feedthrough is further reduced to

$$|v_f| = |v_d| \frac{C_x}{C_s} |\delta_1||\delta_2| \cdot HD_2. \tag{24}$$

It is not difficult to obtain an HD value of .001 with a function generator [4]. The combination of these three techniques (with the previous example values) would reduce a 1 mV feedthrough voltage to 100 pV [4].

2.4 Riehl's Electrometer

In 2003, Riehl *et al.* created a MEMS variable capacitor electrometer [2], [4], [7]. The electrometer was able to detect charges orders of magnitude smaller than the best commercial electrometers. Also, the detection was done at room temperature and atmospheric pressure. Then, in 2008, Lee *et al.* created a MEMS electrometer that could detect an equivalent charge of 6 electrons [3], [5], [6]. His electrometer was made using the same method as Riehl's. Both MEMS electrometers were fabricated using the SOI-MUMPS foundry fabrication process. This requires the devices to be fabricated on a Silicon-On-Insulator (SOI) wafer.

Figure 11 shows a simple schematic of Riehl's electrometer. It is created from a resonating structure that is differentially actuated on both sides by comb-drives.

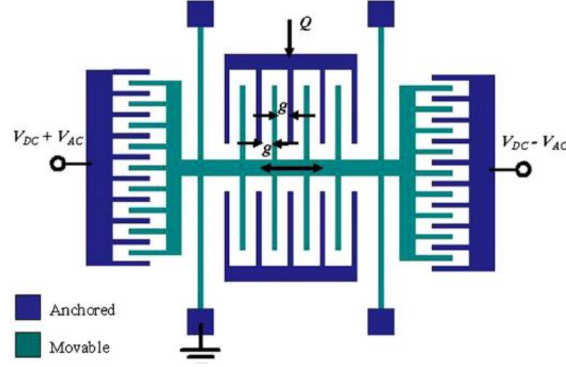

Figure 11. Top view of a simple schematic of a MEMS electrometer (borrowed from [6]).

The middle of the structure is made of alternating stationary and mechanical fingers. As the body resonates at a frequency f, the capacitance between the middle fingers varies at a frequency $2f$. A charge inputed on the top stationary fingers will induce a voltage at $2f$ (charge is only inputted on the top electrodes so that differential sensing can be implemented by subtracting the voltage signal of the bottom electrodes from the sense signal). The difference in frequency between the drive and sense voltage reduces feed-through voltage noise. The induced voltage is equal to [2]

$$V(t) = \frac{Q}{C_V(t) + C_p} \tag{25}$$

where Q is the input charge, $C_V(t)$ is the variable capacitance between the center fingers, and C_p is the parasitic capacitance between the sense node and ground. It can be shown that the RMS voltage component of the output at the frequency $2f$ is

$$V(2f) = Q\frac{C_s}{2\sqrt{2}\left(C_s + C_p\right)^2}\left(\frac{X}{g}\right)^2 \tag{26}$$

were C_s is the stationary capacitance of the variable capacitor, X is the max displacement of the resonator, and g is the initial gap between the sense combs. The resolution of the electrometer is defined as the derivative of the output RMS voltage with respect to the input charge given by [6]

$$Re = \frac{C_s}{2\sqrt{2}\left(C_s + C_p\right)^2}\left(\frac{X}{g}\right)^2. \tag{27}$$

It turns out that for a given X and g, the charge resolution is at a maximum whenever C_p is equal to C_s [6]. The designs of these electrometers limit C_p as much as possible to achieve maximum resolution.

2.5 Riehl's E-field Sensor

Along with the electrometer, Riehl *et al.* also created MEMS electric-field mills (EFMs) [2], [4]. He demonstrated two sensing techniques: one with laterally spaced electrodes and the other with transversely spaced electrodes (depicted in Figure 12). Both methods were created using comb drive actuators and with two sets of electrodes. One set is stationary sense electrodes, and the other is mechanical shutters that are free to oscillate in one direction. Also, both techniques utilized differential drive and sense feedthrough cancelation methods, as discussed in Section 2.3.7. However, neither used harmonic sensing.

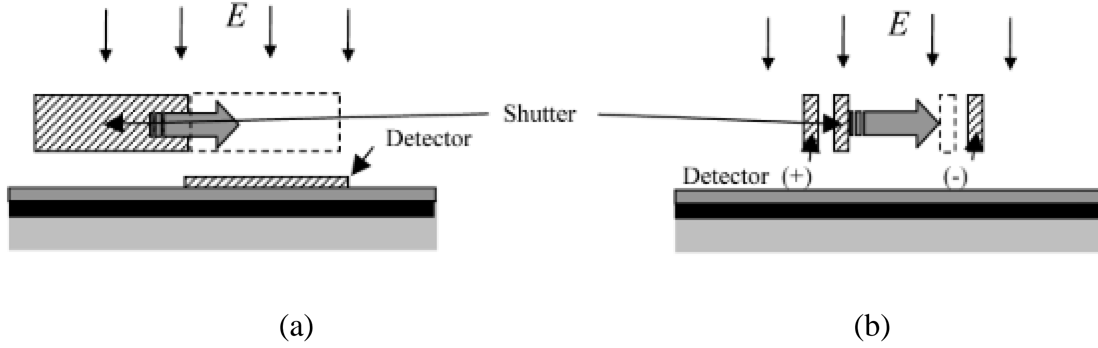

(a) (b)

Figure 12. A depiction of Vertically spaced electrodes (a), and laterally spaced electrodes (b) (borrowed from [2]).

An applied electric field will induce a proportional charge on the sense electrodes. The induced charge is also proportional to the capacitance between the e-field source and sense electrodes. The shutter, while in oscillation, periodically shields and exposes the sense electrodes to the source, creating periodically changing charge or current. In a simple case, the change in capacitance can be expressed as the effective exposed area of the sense electrodes. The current will then be equal to [2]

$$i = \frac{dQ}{dt} = \varepsilon_o |E| \frac{dA}{dt} \tag{28}$$

where ε_0 is the permittivity of free space, $|E|$ is the magnitude of the electric field, and A is the effective area.

2.6 Mechanics

Lateral comb drive resonators electrostatically actuate the device in this research. A typical configuration for the comb drive actuator is shown in Figure 13 (a). There are a pair of combs on the left and right side of a moveable plate. A split dual folded-flexure suspension suspends the plate. When an AC voltage with a DC bias is applied between the

combs, the plate is actuated in a direction parallel to the comb fingers. The resonator can be represented by a mass-spring-damper system (Figure 13 (b)) with an equation of motion given by [12]

$$m\ddot{x} + c\dot{x} + kx = F_e \tag{29}$$

Here, F_e is the electrostatic force on mass m, b is the damping coefficient, k is the spring stiffness of the suspension and, x is the displacement of the mass.

2.6.1 Actuation

The electrostatic force on the left and right combs are $F_{el} = n\frac{\varepsilon t}{g}V_l^2$ and $F_{er} = n\frac{\varepsilon t}{g}V_r^2$ respectively, where n is the number of comb finger pairs on one side, ε is the permittivity of free space, t is the thickness of the fingers, g is the interfinger gap, and V_l and V_r are the left and right side actuation voltages respectively. If $V_l = V_b + V_a \sin \omega t$ and V_r is equal but 180 degrees out of phase, the combined electric force will be

$$\begin{aligned} F_e = F_{el} - F_{er} &= n\frac{\varepsilon t}{g}(V_b + V_a \sin \omega t)^2 - n\frac{\varepsilon t}{g}(V_b - V_a \sin \omega t)^2 \\ &= 4n\frac{\varepsilon t}{g}V_b V_a \sin \omega t = F_0 \sin \omega t \quad \text{where} \quad F_0 = 4n\frac{\varepsilon t}{g}V_b V_a. \end{aligned} \tag{30}$$

V_b, V_a, and ω denote the amplitudes of DC and AC voltage and angular frequency respectively.

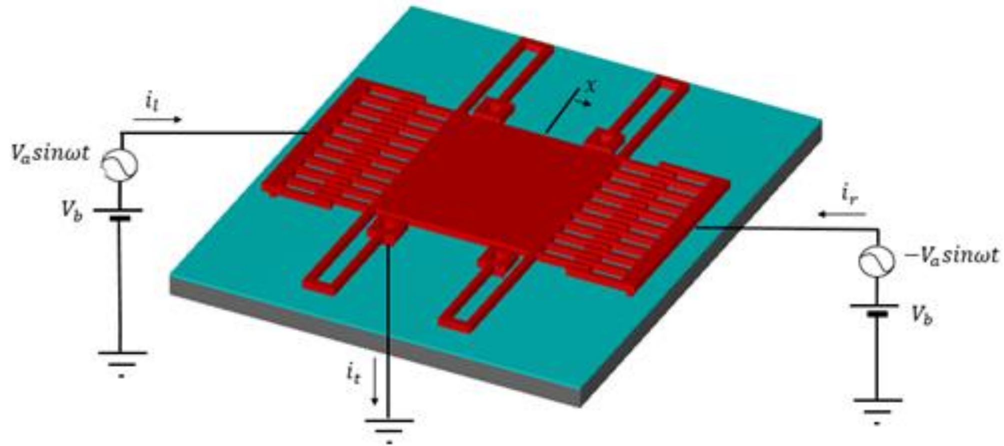

(a)

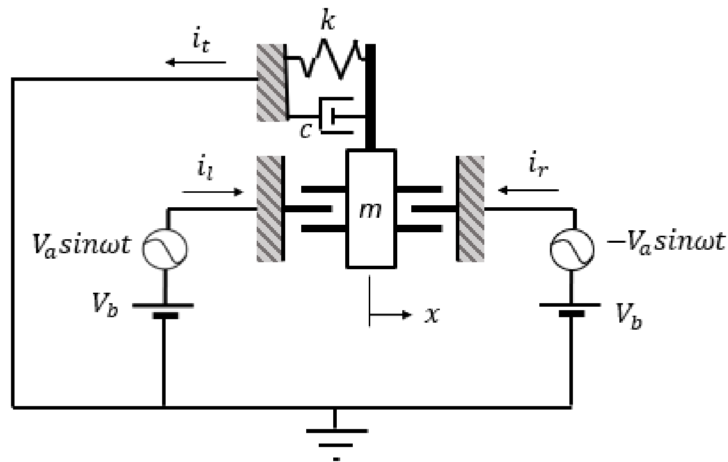

(b)

Figure 13. (a) shows a typical comb drive resonator that is differentially actuated. (b) shows an equivalent mass-spring-damper system of (a).

Substituting Equation (30) into (29) and solving the linear steady-state solution for x gives [12]

$$x = x_0 \sin(\omega t - \phi) \tag{31}$$

where

$$x_0 = \frac{F_0}{k}\frac{1}{\sqrt{(1-\Omega^2)^2 + (\Omega/Q)^2}}$$

$$\Omega = \frac{\omega}{\omega_n} = \frac{f}{f_n}$$

$$\omega_n = \sqrt{\frac{k}{m}} \tag{32}$$

$$\phi = \tan^{-1}\frac{\Omega}{Q(1-\Omega^2)}$$

$$and\ \ Q = \frac{\sqrt{mk}}{c}$$

represent the vibration amplitude, the frequency ratio, the natural frequency, the phase, and the quality factor respectively.

The proceeding solution for the displacement can be used to obtain the current for i_t (Figure 13), which is equal to the sum of i_l and i_r. Since the capacitances on the left and right combs are given by

$$C_l = 2n\frac{\varepsilon t(l-x)}{g} \ \text{ and } \ C_r = 2n\frac{\varepsilon t(l+x)}{g} \tag{33}$$

where l is the initial overlap of the comb fingers, the charge accumulated on each side are

$$Q_l = C_l V_l \ \text{ and } \ Q_r = C_r V_r. \tag{34}$$

Here, charge changes with respect to time which induces currents

$$i_l = V_l\frac{dC_l}{dt} + C_l\frac{dV_l}{dt} = V_l\frac{dC_l}{dx}\frac{dx}{dt} + C_l\frac{dV_l}{dt} = V_l\frac{dC_l}{dx}\dot{x} + C_l\frac{dV_l}{dt} \tag{35}$$

where $\dot{x}$ is the velocity of the mass, and

$$I_r = V_r \frac{dC_r}{dx}\dot{x} + C_r \frac{dV_r}{dt} = -V_r \frac{dC_l}{dx}\dot{x} - C_r \frac{dV_l}{dt}. \tag{36}$$

Adding Equations (35) and (36) gives

$$\begin{aligned} I_t = I_l + I_r = (V_l - V_r)\frac{dC_l}{dx}\dot{x} + (C_l - C_r)\frac{dV_l}{dt} \\ = -(2V_a \sin \omega t)\frac{2n\varepsilon t}{g} x_0 \omega \cos(\omega t - \phi) \\ - \left(\frac{4n\varepsilon t}{g} x_0 \sin(wt - \phi)\right) V_a \omega \cos \omega t \\ = -\frac{4n\varepsilon t}{g} V_a x_0 \omega [\sin(\omega t)\cos(\omega t - \phi) \\ + \cos(\omega t)\sin(\omega t - \phi)] = -\frac{4n\varepsilon t}{g} V_a x_0 \omega \sin(2\omega t - \phi) \end{aligned} \tag{37}$$

Combining the first Equation of (32) with (37) gives

$$-\frac{4n\varepsilon t}{g} V_a \frac{F_0}{k} \omega_n \frac{\Omega}{\sqrt{(1-\Omega^2)^2 + (\Omega/Q)^2}} \sin(2\omega t - \phi). \tag{38}$$

Now adding F_0 from Equation (30) leads to

$$-\left(\frac{4n\varepsilon t}{g}\right)^2 \frac{V_a^2 V_b}{k} \omega_n \frac{\Omega}{\sqrt{(1-\Omega^2)^2 + (\Omega/Q)^2}} \sin(2\omega t - \phi). \tag{39}$$

The resulting solution is a signal at twice the frequency of the drive voltage frequency, meaning harmonic sensing can be used. The amplitude of that signal is at a maximum when the mass is at resonance (i.e., $\Omega = 1$ for $Q \gg 1$). The value of that amplitude is

$$\left(\frac{4n\varepsilon t}{g}\right)^2 \frac{V_a^2 V_b}{k} \omega_n Q = \left(\frac{4n\varepsilon t}{g}\right)^2 \frac{V_a^2 V_b}{c}. \tag{40}$$

Plotting the current amplitude with respect to frequency will give the frequency response of the device. The experiment setup for this is discussed in Chapter 3. It is important to

note that the current amplitude at resonance is sensitive to the damping coefficient c. Therefore, the device could be used as a gas pressure sensor as well.

2.6.2 Suspension

The structural suspension of a MEMS resonator is a critical design parameter. The resonant frequency of the resonator is dependent on the spring constant of the suspension, and it needs to be designed in such a way to minimize out of plane motion. One successful suspension structure is the split dual folded-flexure suspension first demonstrated in MEMS by Tang (Figure 14) [4].

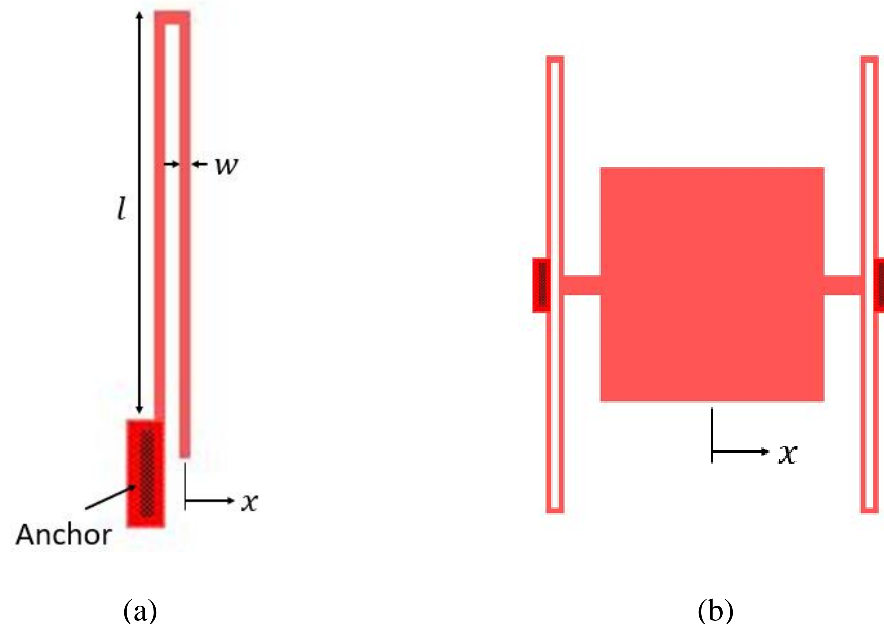

Figure 14. Folded-flexure suspensions: (a) Basic double-folded-flexure suspension, (b) Split dual folded-flexure suspension [4].

This design was shown to have a primary resonant frequency that was five times smaller than any other in-plane mode [4]. The primary spring constant in the x-direction, k_x, is given by [4]

$$k_x = \frac{2Ehw^3}{L^3} \tag{41}$$

where E is the Young's modulus, h is the thickness of the structure, w is the width of the beam, and L is its length. All of the structures in this research were designed with this suspension. Nonlinear spring stiffening becomes significant when the displacement exceeds ten percent of the beam length [4]. Careful consideration was made so that the displacement does not exceed that threshold.

2.6.3 Damping

A restoring force, damping, resists the movement of a body through a fluid. The force is equal to the velocity of the body times a damping coefficient c (as seen in Equation (29)). For MEMS structures, there are two major models for damping: Squeeze film damping and Couette flow or slide-film damping.

Squeeze film damping occurs between two parallel plates that move in a direction perpendicular to each other (Figure 15 (a)). With an array of n plates with area A, width z, and initial gap y; the damping coefficient due to squeeze-film damping will be equal to

$$c_{sq} = n\mu \frac{7Az^2}{y^3} \tag{42}$$

where μ is 18.5 μPa·s, the viscosity of air [13]. Couette flow models the damping of two parallel plates that move transversely with respect to each other (Figure 15 (b)). The damping coefficient due to Couette flow is equal to [13]

$$c_{cf} = n\mu \frac{A}{y}. \tag{43}$$

By adding Equations (42) and (43), we can estimate the damping coefficient of the system. For the device in this research, Couette flow is the dominant force of damping (as in the majority of micromachined devices that move transversely with respect to the substrate).

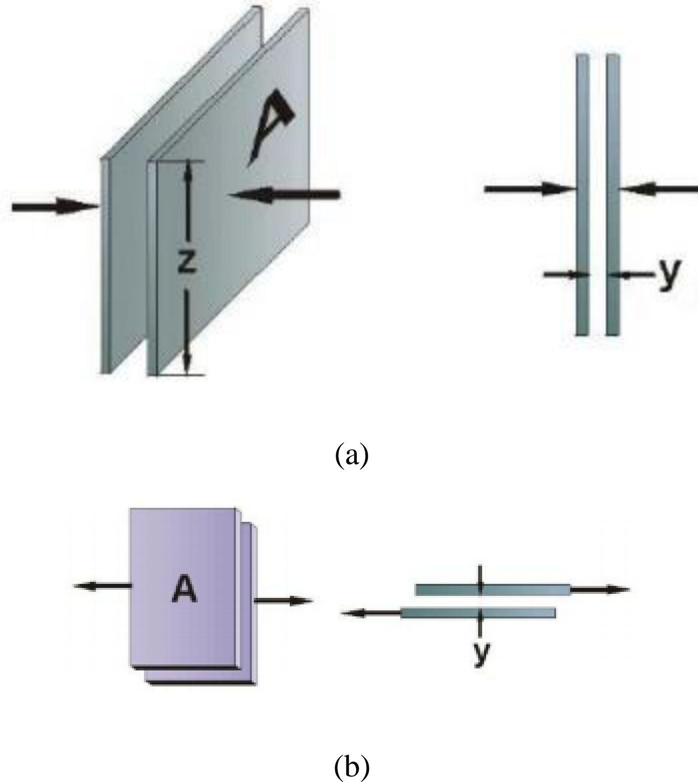

(a)

(b)

Figure 15. Depictions of squeeze film damping (a) and slide film damping (b) (borrowed from [13]).

2.7 Conclusion

Tables 1 and 2 give a short survey of several MEMS e-field sensors and electrometers. Some of these devices are force based electrometers. They have added advantages over variable capacitor sensors in that they are smaller, not as affected by damping, and the charge resolution is not dependent on parasitic capacitance. However, they are not as sensitive.

From studying the difference between Riehl's lateral and vertical EFM, the vertical EFM has a smaller damping coefficient even with a much greater mass. Granted, the lateral EFM is affected by both squeeze film and slide film damping (not just slide film) since a backside release was not done on these devices; but given the much smaller mass, the smaller quality factor, and Equations (38) and (39), I conclude that squeeze film damping has a harsher damping effect. So, to reduce damping effects, this research asks the question, "what if we create a vertical electrometer."

This research also tests the vertical electrometer's ability to measure an electric field. The uniqueness between our EFM and others is that ours utilizes harmonic sensing instead of differential sensing.

Also, another disadvantage of previous devices is that they utilized a microforming fabrication techniques on SOI wafers. SOI wafers are much more expensive than, standard silicon wafers. This research uses a proven, well established, and cost-effective micromachining technique using standard silicon wafers.

All of the sources of noise need to be considered for designing electrostatic charge and field sensors. Among the most sensitive are variable capacitor MEMS devices. These devices suffer greatly from access size and damping. Vertically transverse MEMS devices tend to be less damped than laterally transverse MEMS. This research developed a method for utilizing a vertically traverse configuration to detect charge. The next section develops the methodology for creating and testing these devices, as well as it develops the mathematical theory of their response to electrostatics.

Table 1. Review of MEMS Electrometers

Reference	Charge sensing type	Transduction principle	Functional materials	Fabrication technology	Temp-erature	Pressure	Resolution
[14]	NEMS torsional resonator	Magnetomotive actuation and detection	SOI	EBL	4.2 K	< mTorr	1E-6 e $Hz^{-1/2}$ *
[15]	NEMS translational resonator	Magnetomotive actuation and detection	SOI	EBL + RIE	4.2 K	1.3 Torr	70 e $Hz^{-1/2}$
[16]	NEMS translational resonator	Electrical/optical actuation and optical interferometer detection	Graphene	Mechanical exfoliating	300K	$<10^{-6}$ Torr	8E-4 e $Hz^{-1/2}$
[17]	NEMS translational resonator	Electrostatic actuation and tunneling detection	SW/NT	NEMS + SET	50 mK	-	0.97E-6 e $Hz^{-1/2}$
[18]	MEMS translational resonator	Electrostatic actuation and detection	SOI	Bulk Micromachining (MEMSCAP)	300 K	4 mTorr	4 fC
[19]	MEMS translational resonator	Electrostatic actuation and detection	SOI	Bulk Micromachining (MUMPS)	300 K	40 mTorr	21 fC
[20]	MEMS translational resonator	Electrostatic actuation and detection	SOI	Bulk Micromachining (MUMPS)	300 K	-	0.84 fC
[21]	MEMS weakly coupled resonator	Electrostatic actuation and detection	SOI	Surface Micromachining	300 K	20 mTorr	1.269 fC
[2]	MEMS vibrating-reed	Electrostatic actuation and detection	SOI	Surface Micromachining (ModMEMS)	300 K	Ambient (air)	28 e @ 0.3 Hz
[22]	MEMS vibrating-reed	Electrostatic actuation and detection	SOI	Bulk Micromachining (MEMSCAP)	300 K	Ambient (air)	524 e $Hz^{-1/2}$
[3]	MEMS vibrating-reed	Electrostatic actuation and detection	SOI	Bulk Micromachining (MEMSCAP)	300 K	Ambient (air)	6 e $Hz^{-1/2}$
[9]	MEMS vibrating-reed	Electrostatic actuation and detection	SOI	Bulk Micromachining (ThELMA)	300 K	Ambient (air)	23 e $Hz^{-1/2}$

Table 2. Review of MEMS Electric Field Sensors

Reference	E-field sensing type	Transduction principle	Functional materials	Fabrication technology	Tempe -rature	Pressure	Resolution
[23]	Vertical EFM	Electrostatic actuation and detection	-	Surface Micromachining	300 K	< mTorr	1600 V/m
[11]	Vertical EFM	Thermal actuation and electrostatic detection	Poly-silicon	Surface Micromachining (PolyMUMPs)	-	Ambient (air)	101.7 V/m
[10]	Vertical EFM	Electrostatic actuation and detection	Poly-silicon	Surface Micromachining (PolyMUMPs)	300 K	Ambient (air)	100 V/m
[24]	Lateral EFM	Electrostatic actuation and detection	SOI	Bulk Micromachining (SOIMUMPs)	300 K	Ambient (air)	50 V/m
[25]	Lateral EFM	Electrostatic actuation and detection	SOI	Bulk Micromachining	300 K	Ambient (air)	-
[2]	Vertical EFM	Electrostatic actuation and detection	SOI	Surface Micromachining (ModMEMS)	300 K	Ambient (air)	4900 V/m
[2]	Lateral EFM	Electrostatic actuation and detection	SOI	Surface Micromachining (ModMEMS)	300 K	Ambient (air)	630 V/m
[26]	Vertical EFM	Electrostatic actuation and detection	Poly-silicon	Surface Micromachining (iMEMS)	300 K	Ambient (air)	4 V/m $Hz^{-1/2}$
[27]	Optically tracked mechanical displacement of a spring-suspended seismic mass	Passive actuation and optical detection	SOI	Surface Micromachining	300 K	Ambient (air)	100 V/m $Hz^{-1/2}$

III. Theory and Methodology

3.1 Chapter Overview

This research developed a dual sensor that can function as an electrometer and as an electric field mill (EFM). The device was fabricated by MEMSCAP using the PolyMUMPs process. It is made up of a layer of stationary bottom, sense electrodes and a layer of mechanical, grounded electrodes. Both layers are patterned into a grill structure with four-micrometer wide electrodes and four micrometer wide gaps between each one. The two layers are perfectly misaligned so that none of the electrodes overlap each other (Figure 16).

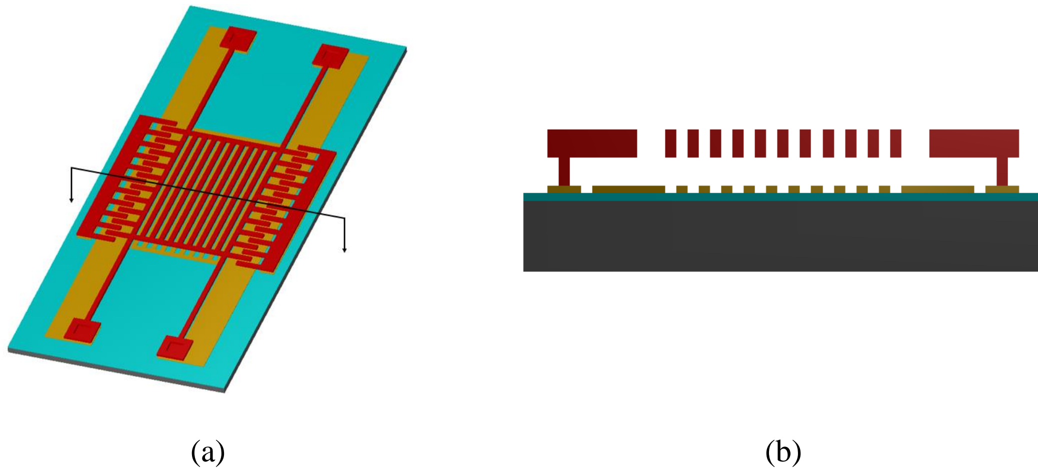

(a) (b)

Figure 16. (a) shows a simple 3D model of the dual sensor design. (b) shows the cross section of (a).

This chapter lays out the methodology of testing these devices. First, electromechanical tests were performed to optimize the displacement and actuation voltages used. Then, the electrometer mode was tested. A charge was induced through a test capacitor at the sense node. If the test capacitance is much smaller than the capacitance of the device, then the

charge on the sense node will be equal to the voltage at the input of the test capacitor times its capacitance. Finally, the EFS mode was tested. An electric field was created from a source electrode that is placed a known distance above the device. The induced electric field is normal to the device and proportional to the voltage on the test electrode. This chapter also derives the theoretical models of the responsivities for each mode, and it develops noise models for both.

3.2 Fabrication

The device was fabricated by MEMSCAP using the PolyMUMPs foundry process (Figure 17). The PolyMUMPs process creates three highly doped, poly-silicon layers; two are mechanical device layers.

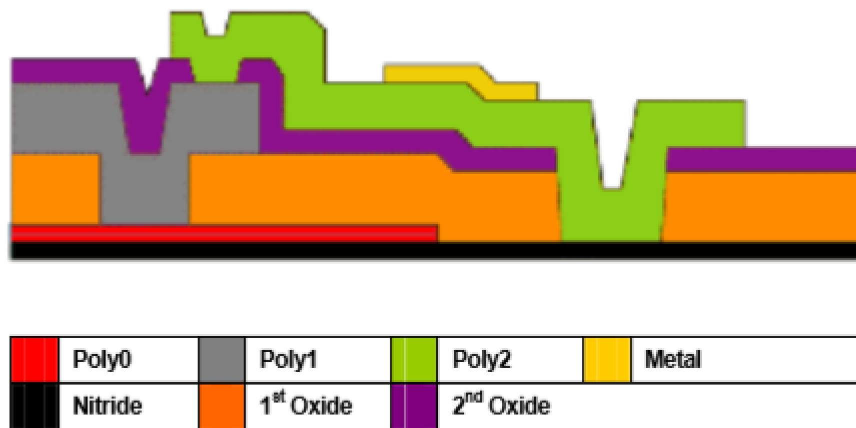

Figure 17. A cross section view showing all seven layers of the PolyMUMPs Process [28].

PolyMUMPs is an eight-mask process. First, 0.6 micrometers of silicon nitride is deposited on a standard n-type (100) silicon wafer. The nitride layer is a good insulator and reduces leakage current. Next, the first polysilicon layer (poly-0) is deposited and patterned

using lithography and plasma etching. The poly-0 layer is 0.5 micrometers thick. Then a 2-micrometer thick buffer oxide layer is deposited on top of the poly-0. Lithography and reactive-ion etching are used to create 0.75 micrometer deep dimples into the oxide. The dimples prevent stiction of the second polysilicon layer to the substrate. Then, the oxide layer is patterned to create anchors for the next poly-silicon layer to either the nitride or poly-0. Next, 2 micrometers of poly-silicon (poly-1) is deposited over the oxide, doped, and then lithographically etched using plasma processing. Following the poly-1 etch, the second buffer oxide layer (0.75 micrometers thick) is deposited onto the wafer. This layer is patterned twice: the first creates anchors to the poly-1 layer and the second to the nitride or poly-0 layer. Then the last poly-silicon layer (poly-2) is deposited, doped, and patterned. The layer is 1.5 micrometers thick. Finally, 0.5 micrometers of gold is deposited and patterned using lift-off. The gold layer is used for probing, bonding, and electrical routing. At the end of the process, the wafer is coated with photoresist and diced. The devices were released in the AFIT cleanroom. This required a 4 min HF buffer oxide etch followed by a critical point dry.

The device was designed to create a large variation in capacitance with a resonant frequency that exceeds the 1/f noise corner of the JFET buffer. JFETs typically have a noise corner around 100 Hz. The device has a calculated resonant frequency of 16.65 kHz, well above the noise corner. Calculated parameter values are shown in Table 3. The variation in capacitance was highly overestimated during device design because fringing capacitance was ignored. Table 3.1 shows a realistic estimation

Table 3. Design Parameters of Electrometer/EFM

Parameter	**Calculated value based on design dimensions**
Mechanical part film thickness (μm)	2
Suspension beam length l_s (μm)	135
Suspension beam width w_s (μm)	3
Spring constant (folded beam in N/m)	6.13
Structure mass (μg)	0.56
Resonant Frequency (kHz)	16.65
Drive comb gap g_d (μm)	3
Number of drive combs (each side) n_d	40
DC Voltage (V)	80
AC Voltage (Vpp)	16
dC/dx of drive combs (each side, in F/m)	9.44E-10
Sense electrode gap g (μm)	2
Sense electrode length l_s (μm)	150
Number of sense electrodes n_s (each side)	70
Displacement amplitude $\hat{x}$ (μm)	4
Damping Coefficient (N·s/m)	1.14E-6
Quality Factor	51.28
Parameter	**Calculated value based on design dimensions**
Maximum Capacitance C_{max} (between sense electrodes and mechanical mass in pF, each side)	0.186
Static capacitance $C_0 + C_{f0}$ (between sense electrodes and mechanical mass in pF)	0.25 (simulated)
Change in fringing capacitance ΔC_f (between sense electrodes and mechanical mass in pF, each side)	-0.155 (simulated)
Change in total capacitance ΔC (between sense electrodes and mechanical mass in pF, each side)	0.033 (simulated)

3.3 Electromechanical Characterization

Several electromechanical factors needed to be measured. These factors help determine the optimal voltage settings to actuate the multimeter. One of the factors is the dependence

on maximum displacement (at resonance) with respect to drive voltage. This response, theoretically, is linear. However, spring stiffening will cause the response to be nonlinear at larger displacements. The device under test (DOT) was designed to operate within the linear region; which for a folded beam suspension is 10 percent of the beam length [4]. In our case, the beam length is 135 micrometers, and the optimal displacement is 4 micrometers, so there were no observed nonlinearities. Other factors are the air gap distance between the top electrodes and bottom, and the width of each electrode. The electrodes are designed to be 4 micrometers wide, but the width ultimately decreases during fabrication [9]. These dimensions were measured with a 3D microscope. Finally, the frequency response and quality factor were measured.

Figure 18 shows the experimental setup for testing the electromechanical characterization. The DOT is electrostatically actuated using a push-pull technique. This is done by applying two anti-phase AC signals, one on each side of the comb-drive resonator. Each side is also superimposed with the same DC bias. As discussed in Section 2.6.1, the current I3 has a resonant amplitude equal to

$$\left(\frac{dC}{dx}\right)^2 \frac{VbVa^2}{k} \omega_n Q = \left(\frac{dC}{dx}\right)^2 \frac{VbVa^2}{c} \tag{44}$$

at twice the frequency of the actuation voltage. In the above Equation, $\frac{dC}{dx}$ is the capacitance sensitivity, V_a is the amplitude of the two AC voltage signals, V_b is the DC bias voltage, Q is the quality factor, ω_n is the resonant frequency, k is the effective spring constant, and c is the damping coefficient.

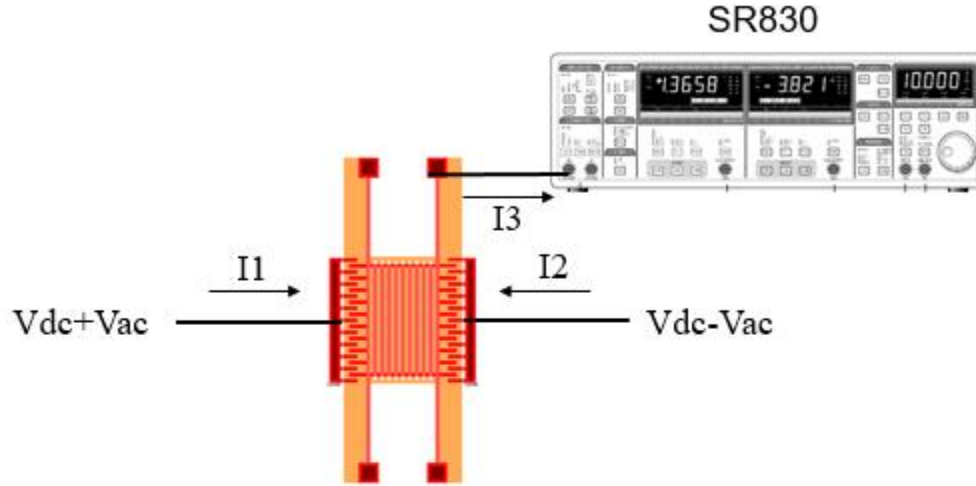

Figure 18. Experimental setup for mechanical characterization.

V_a, V_b, Q, w_n, and k are all either known or can be calculated from the frequency response. $\frac{dC}{dx}$ should theoretically equal 9.44E-10 F/m (according to Equation (40)). This value cannot be assumed, because the drive comb gaps and overlaps will differ from the designed dimensions due to the reduction in line width [9]. However, $\frac{dC}{dx}$ can be calculated from Equation (44), or it can be estimated based on measurements. We have done both in this experiment.

The above analysis will hold as long as the quality factor is much larger than one ($Q >> 1$). If not (i.e., $Q < 10$), the resonant frequency, ω_r, will be related to the natural resonance, ω_n, by the relation [29]:

$$\omega_r = \omega_n\sqrt{1 - \frac{1}{2Q^2}}, \text{ where } \omega_n = \sqrt{\frac{k}{m}} \tag{45}$$

and m is the effective mass of the system. Then, the magnitude of I3 at resonance would equal

$$\left(\frac{dC}{dx}\right)^2 \frac{VbVa^2}{k} \omega_n Q \left(\frac{1-\frac{1}{2Q^2}}{1-\frac{1}{4Q^2}}\right)^{\frac{1}{2}} = \left(\frac{dC}{dx}\right)^2 \frac{VbVa^2}{c} \left(\frac{1-\frac{1}{2Q^2}}{1-\frac{1}{4Q^2}}\right)^{\frac{1}{2}} \tag{46}$$

and the same calculations can be made to solve for the electromechanical characteristics.

3.4 Electrometer Sensitivity Analysis

The electrometers in this research utilize harmonic sensing to reduce the noise of the feed-through signal. The electrometer does this by modulating the charge voltage between the grounded resonator and the sense electrodes to even harmonics of the drive signal. A lock-in amplifier was used to measure the RMS voltage at the second harmonic of the output. This section derives the equation for the second harmonic voltage of the resonator.

The electrometer is differentially actuated in the x-direction by comb drive actuators. The resonating part is made up of several grounded electrodes. Each one of the electrodes is surrounded by a bottom electrode as seen in Figure 19 (c) and (d). We examined the voltage response of one of these electrodes to derive the charge conversion gain.

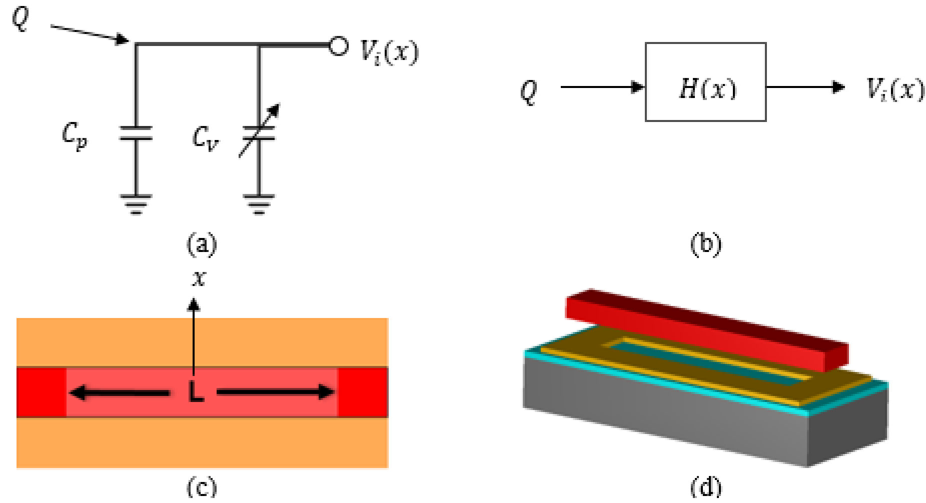

Figure 19. This figure shows conceptual pictures of the variable capacitor. (a) shows a simplified circuit where C_p is the lumped up parasitic capacitances, C_v is the variable capacitor, and Q is the charge that induces the sense voltage V_i. (b) is a block diagram of the same circuit. (c) is a 2D model of one electrode. (d) is a 3D model of (c) [30].

Figure 19 (a) shows a simplified circuit representation of the electrometer, where C_p is the parasitic capacitance, and C_v is the variable capacitor. The charge, Q, is applied to the input node of the device resulting in an AC voltage, V_i, due to the variable capacitance. A block diagram representation of this circuit is shown in Figure 19 (b) with the transfer function

$$\mathrm{H(x)} = \frac{V_i(x)}{Q} = \frac{1}{C(x)} \text{ where } C(x) = \frac{\epsilon_o L x(t)}{g} + C_o + C_p \text{ and } x(t) = |\hat{x}\sin(\omega t)|. \tag{47}$$

ϵ_o is the permittivity of free space and g is the gap between the two electrodes. The area between the two electrodes is equal to the length L times the displacement $x(t)$ plus a constant area (represented by the dark color red in Figure 19 (d)). The constant area induces

a static capacitance denoted by C_o. The displacement is sinusoidal with an amplitude $\hat{x}$. Since both positive and negative displacement increases the area, the variable capacitance is related to the absolute value of the displacement. Substituting $x(t)$ and rearranging results in

$$C(t) = \frac{\epsilon_o L\hat{x}|\sin(\omega t)|}{g} + C_{po} = \frac{\epsilon_o L\hat{x}}{g}(|\sin(\omega t)| + \frac{C_{po} g}{\epsilon_o L\hat{x}}). \tag{48}$$

If we assign the variables C_{max} and α as

$$C_{max} = \frac{\epsilon_o L\hat{x}}{g} \text{ and } \alpha = \frac{C_{po} g}{\epsilon_o L\hat{x}} = \frac{C_{po}}{C_{max}} \tag{49}$$

the transfer function, with respect to time, will be equal to

$$H(t) = \frac{1}{C_{max}(|\sin(\omega t)| + \alpha)}. \tag{50}$$

Equation (47) shows that the output voltage divided by the input charge is equal to the transfer function. It is also true that the derivative of the voltage taken with respect to Q is equal to the transfer function. This derivative is equal to the responsivity of the sensor (denoted as $\frac{d\bar{v}_i}{dQ}$). To find the responsivity at the second harmonic of the output voltage, we perform a Fourier series expansion on Equation (50):

$$H(t) = \frac{a_o}{2} + \sum_{n=1}^{\infty} a_n \cos(nt) + b_n \sin(nt) \text{ where } a_n = \frac{2}{P}\int_{t_o}^{t_o+P} H(t)\cos\left(\frac{2\pi nt}{P}\right) dt. \tag{51}$$

Here, when n is equal to two, a_n is equal to the change in amplitude per charge at the second harmonic. Since $H(t)$ is an even function, the sin product in the summation can be ignored. Solving for a_n gives [30]

$$a_2 = \frac{\omega}{\pi C_{max}} \int_{-\pi/\omega}^{\pi/\omega} \frac{\cos(2\omega t)dt}{|\sin(wt)|+\alpha} = \frac{2\omega}{\pi C_{max}} \int_{0}^{\pi/\omega} \frac{\cos(2\omega t)dt}{\sin(wt)+\alpha} = \frac{2}{\pi C_{max}} \int_{0}^{\pi} \frac{\cos(2\tau)d\tau}{\sin(\tau)+\alpha} =$$

$$\frac{2}{\pi C_{max}}\left(2\alpha\pi - 4 - \frac{(4\alpha^2-2)\tan^{-1}(\sqrt{\alpha^2-1})}{\sqrt{\alpha^2-1}}\right). \tag{52}$$

The integral was solved empirically, and the numerical results agree with MATLAB calculations for small values in α. When α is large (i.e. α > 5E4) Equation (52) becomes unstable. The actual measurement taken is the RMS value of the second harmonic, which is

$$\frac{d\bar{v}_{i\,rms}}{dQ} = \frac{\sqrt{2}}{\pi C_{max}}\left(2\alpha\pi - 4 - \frac{(4\alpha^2-2)\tan^{-1}(\sqrt{\alpha^2-1})}{\sqrt{\alpha^2-1}}\right). \tag{53}$$

This result does not consider the fringing capacitance between the top and bottom electrodes. To compensate, we add a correction to Equation (53) [30].

$$\frac{\boldsymbol{d\bar{v}_{i\,rms}}}{\boldsymbol{dQ}} = \frac{\sqrt{2}}{\pi(C_{max}+\Delta C_f)}\left(2\alpha\pi - 4 - \frac{(4\alpha^2-2)\tan^{-1}(\sqrt{\alpha^2-1})}{\sqrt{\alpha^2-1}}\right)\ where\ \alpha = \frac{C_{p0}+C_{f0}}{C_{\max}+\Delta C_f}. \tag{54}$$

C_{f0} is the initial value of the fringing capacitance (when x is equal to zero) and ΔC_f is the change in fringing capacitance. These two values were simulated in COMSOL. Equation (54) assumes that the change in fringing capacitance is linear with respect to x (same as the overlap capacitance). This assumption was made from initial simulations.

3.5 Electrometer Noise Analysis

The dominant noise sources in the electrometer circuit are in-band noise sources. In-band noise is generated at the sense frequency, as oposed to up-mixed noise that is generated at a lower frequency then up-mixed to the sense frequency. The significant noise

sources in the electrometer are the in-band thermal noise of resistors and transistors, 1/f noise of transistors, and the up-mixed shot noise at the input of the buffer [4].

Figure 20 shows the noise model of the electrometer. R_w represents the parasitic wiring noise between the variable capacitor and the input of the buffer. The resistance induces a thermal noise represented by $\bar{v}_{nr}$. The gains of the buffer and the gain stage in the circuit are represented by A_b and A_g respectively. The input referred voltage noise of each are represented by $\bar{v}_{nb}$ and $\bar{v}_{ng}$.

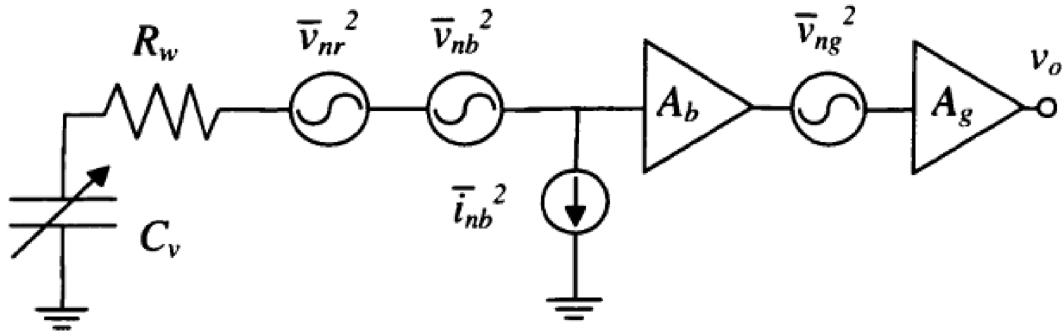

Figure 20. Noise model of the Electrometer [4].

The in-band variance of the circuit is calculated from the spectral densities of these noise sources as [4]

$$\bar{v}_{ni}^2 = \left[\left(\frac{\bar{v}_{nr}^2}{\Delta f} + \frac{\bar{v}_{nb}^2}{\Delta f}\right) A_b^2 + \frac{\bar{v}_{ng}^2}{\Delta f}\right] A_g^2 f_c \tag{55}$$

where f_c is the detection bandwidth of the lock-in amplifier. The in-band charge noise is found by dividing Equation (55) by (54), the charge conversion gain of the electrometer, and the gain of the circuit, $A_b A_g$ [4].

$$\bar{Q}_{ni}^2 = \left(\frac{d\bar{v}_i}{dQ}\right)^{-2} \left[\frac{\bar{v}_{nr}^2}{\Delta f} + \frac{\bar{v}_{nb}^2}{\Delta f} + \frac{\bar{v}_{ng}^2}{\Delta f}\frac{1}{A_b^2}\right] f_c \tag{56}$$

We also considered up-mixed noise from gate current shot noise represented by $\bar{\iota}_{nb}$. The charge noise generated by the gate current is given in Equation (8) and below as [4]

$$\bar{Q}_{nu}^2 = \frac{1}{4\pi^2 f_s}\frac{\bar{\iota}_{nb}{}^2}{\Delta f}. \tag{57}$$

The up-mixed voltage noise is equal to Equation (57) times the gain of the circuit and the charge conversion gain [4].

$$\bar{v}_{nu}^2 = \frac{1}{4\pi^2 f_s}\frac{\bar{\iota}_{nb}{}^2}{\Delta f}\left(\frac{d\bar{v}_i}{dQ}\right)^2 A_b^2 A_g^2 \tag{58}$$

The resolution of the electrometer is given by the square root of the sum of Equations (56) and (57) as listed below [4]:

$$\bar{Q}_n = \sqrt{\left(\frac{d\bar{v}_i}{dQ}\right)^{-2}\left[\frac{\bar{v}_{nr}^2}{\Delta f} + \frac{\bar{v}_{nb}^2}{\Delta f} + \frac{\bar{v}_{ng}^2}{\Delta f}\frac{1}{A_b^2}\right] f_c + \frac{1}{4\pi^2 f_s}\frac{\bar{\iota}_{nb}{}^2}{\Delta f}}. \tag{59}$$

The square root of the sum of Equations (55) and (58) give the total RMS output noise voltage of the system [4]:

$$\bar{v}_n = \sqrt{\left[\left(\frac{\bar{v}_{nr}^2}{\Delta f} + \frac{\bar{v}_{nb}^2}{\Delta f}\right) A_b^2 + \frac{\bar{v}_{ng}^2}{\Delta f}\right] A_g^2 f_c + \frac{1}{4\pi^2 f_s}\frac{\bar{\iota}_{nb}{}^2}{\Delta f}\left(\frac{d\bar{v}_i}{dQ}\right)^2 A_b^2 A_g^2}. \tag{60}$$

3.6 Experimental Setup of Electrometer

We used an SR830 lock-in amplifier to measure the output voltage of the MEMS resonator. An Agilent 33250A function generator and two wideband power amplifiers were used to actuate the MEMS device. The amplifiers outputted AC signals that were 180 degrees out of phase from each other and coupled to a DC bias. The values of the actuation frequency, AC amplitude, and DC bias were all chosen from the electromechanical tests

described in Section 3.3 and are shown in Table 3. We used the output of the Agilent 33250A as the lock-in reference frequency. The lock-in amplifier amplifies the output signal and uses phase sensitive demodulation to measure the second harmonic component of the signal. The SR830 also supplied the test voltage, v_t, from one of its AUX voltage outputs on the back of the machine (not shown in Figure 21). The test voltage was coupled to the sense node through a test capacitor, C_t. A DC voltage on the test capacitor will induce a DC charge on the sense node by the relation $Q = V_t C_t$. A step function is used as the test voltage, where each step is larger than the last. The output of the electrometer is proportional to the charge induced by the relation given in Equation (54).

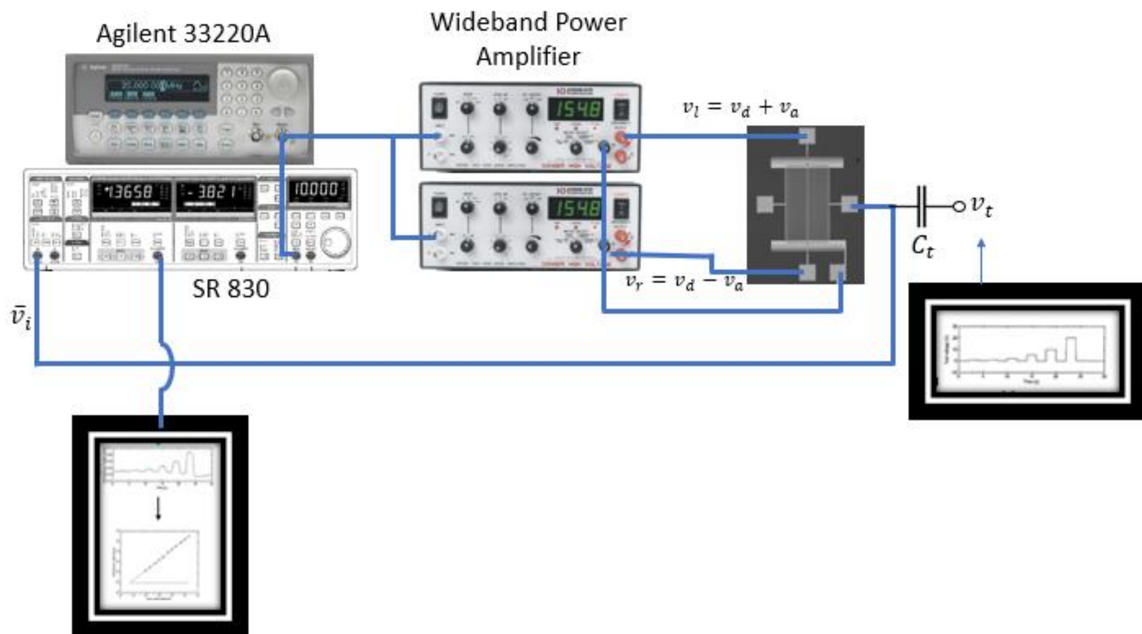

Figure 21. Experimental Setup for testing the electrometer mode.

The device itself was placed in a ceramic package and wire bonded to external connections. While testing, the package was placed inside a metal Faraday cage with external connections. This reduces noise sources from the surrounding environment.

3.7 Electric Field-Mill Sensitivity Analysis

In the EFM, the electric field is modulated into an AC signal. This is done with two sets of electrodes (Figure 22). The first is a set of stationary sense electrodes, and the second is grounded shutters that periodically shield and expose the sense electrodes.

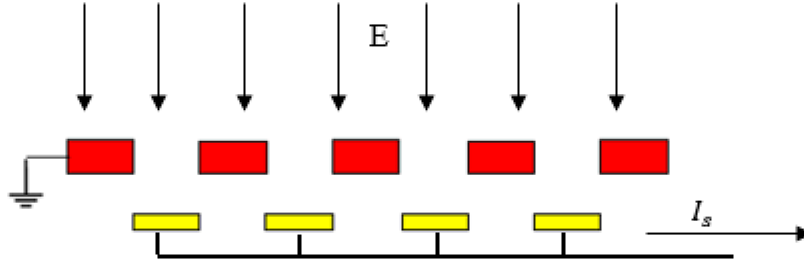

Figure 22. Cross section of the shutter and sense electrodes while in EFS mode.

The electric field (EF) induces a charge that is proportional to the EF and the exposed area of the sense electrodes. Since the area, therefore the charge, changes with respect to time, a current is induced and is equal to [2]

$$I_s = \frac{dQ_i}{dt} = \varepsilon_0 |E| \frac{dA}{dt} \tag{61}$$

where Q_i, ε_0, $|E|$, and A are the induced charge, permittivity of free space, perpendicular EF, and the exposed area of the sense electrodes respectively. It is assumed that the EF is perpendicular to the sense electrodes. This is a reasonable assumption since the source electrode will be kept far from the DOT (in the order of hundreds of micrometers).

The exposed area is a function of the shutter displacement by the relation

$$A = nL(w - |x|) \tag{62}$$

where n is the number of sense electrodes, L is their length, w is their width, and |x| is the absolute value of the shutter displacement. $\frac{dA}{dt}$ can also be written as $\frac{dA}{dx}\frac{dx}{dt}$. Solving $\frac{dA}{dx}$ and substituting it into Equation (61) yields

$$I_s = -\varepsilon_0 |E| nL \frac{x}{|x|}\frac{dx}{dt}. \tag{63}$$

Since $x = x_0 \sin(\omega t)$, the induced current will be

$$\begin{aligned} I_s &= -\frac{\varepsilon_0 |E| nl\omega x_o \sin(\omega t)\cos(\omega t)}{|\sin(\omega t)|} = -\frac{\varepsilon_0 |E| nL\omega x_o \sin(2\omega t)}{2|\sin(\omega t)|} \\ &= -\frac{\pi K |E| \sin(2\omega t)}{|\sin(\omega t)|} \end{aligned} \tag{64}$$

where $K = \varepsilon_0 nLf x_o$.

The current signal is analyzed with a lock-in amplifier. First, the lock-in amplifier converts the current into a voltage with an amplification of A_g. Then, it measures the rms amplitude of the 2ω component of the voltage signal. Here, ω is the reference frequency of the lock-in amplifier, which is the same frequency of the drive voltage used to actuate the DOT. A Fourier series expansion was done on Equation (64). The rms amplitude of the 2ω component is

$$\overline{I_s} = \frac{8\sqrt{2}K}{3}|E| \tag{65}$$

The electric field responsivity of the DOT can then be expressed as

$$\frac{d\overline{v_s}}{d|E|} = \frac{d\overline{\iota_s}}{d|E|}\frac{dv_s}{di_s} = \frac{d\overline{\iota_s}}{d|E|}A_g = \frac{8\sqrt{2}K}{3}A_g. \tag{66}$$

That is, for every volt-meter increase in electric field, the RMS output voltage will increase by $\frac{8\sqrt{2}K}{3}A_g$.

3.8 Electrostatic Field-Mill Noise Analysis

Just like the electrometer, we need to consider the in-band noise in the EFM circuit (Figure 24). These are created by the thermal noise of the feedback resistor, $\bar{v}_{nr}$, and the 1/f noise of both the trans resistance amplifier (TRA) and gain stage, $\bar{v}_{n1}$ and $\bar{v}_{n2}$ respectively.

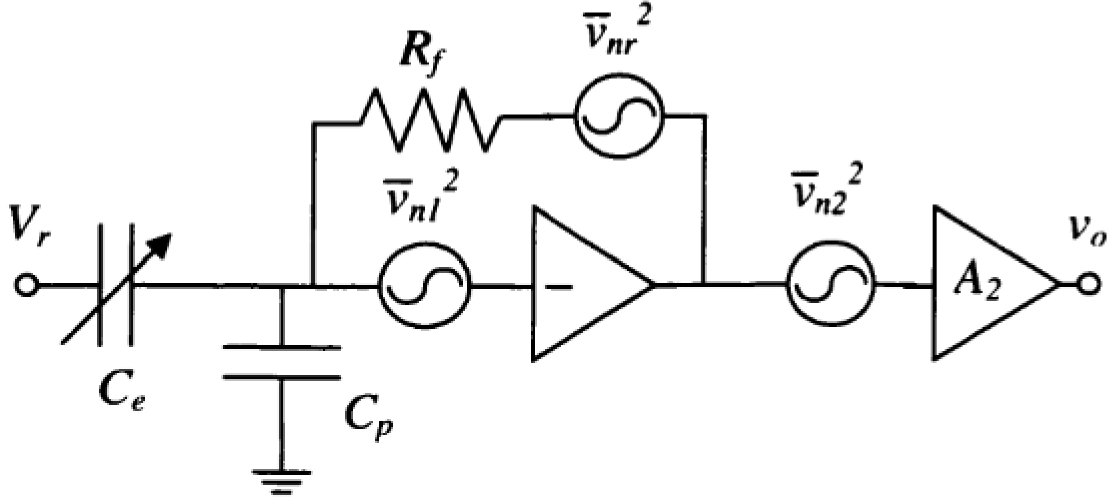

Figure 23. Noise model of EFS (Borrowed from [4]).

We also need to consider up-mixed noise, as discussed in Section 2.3.6. To analyze the up-mixed noise, we compare Figure 6 and Figure 23, then make the following substitutions [4]:

$$Z_i = \frac{1}{sC_e} \qquad Z_p = \frac{1}{sC_p}$$
$$Z_f = R_f \qquad V_n = V_{nl} \tag{67}$$

which gives the noise transfer function [4]

$$NTF = 1 + s(C_e + C_p)R_f. \tag{68}$$

Here C_e is the change in capacitance between the source and the detector. Using Equation (62) and the value of x, the variable capacitance can be written as

$$C_e = \frac{\varepsilon_0 nLw}{g_{sd}} - \frac{\varepsilon_0 nLx_0|\sin(\omega t)|}{g_{sd}} \quad (69)$$

where g_{sd} is the source to detector gap. Substituting Equation (69) into (68) and isolating the time varying components gives the NTF of the up-mixed noise, which is

$$NTF_u = -s\frac{R_f \varepsilon_0 nLx_0|\sin(\omega t)|}{g_{sd}}. \quad (70)$$

The 2ω component is calculated from a Fourier series expansion and has a magnitude of

$$\overline{NTF_u} = \omega\frac{4}{3\pi}\frac{R_f \varepsilon_0 nLx_0}{g_{sd}}. \quad (71)$$

given the parameters in table 3.1 and an $R_f = 1\text{k}\Omega$, $\overline{NTF_u}$ is equal to 4.3×10^{-6}. This means that for every DC volt at the input of the TRA, there will be 4.3×10^{-6} volts at the output sense frequency. Since the in-band noise has an NTF of nearly unity, the up-mixed noise can be ignored. The total noise in the system is the added noise of the in-band sources times the gain of the amplifier. The noise spectral density is [4]

$$\frac{\bar{v}_n^2}{\Delta f} = A_2^2\left[\frac{\bar{v}_{n1}^2}{\Delta f} + \frac{\bar{v}_{nr}^2}{\Delta f} + \frac{\bar{v}_{n2}^2}{\Delta f}\right]. \quad (72)$$

To find the EF resolution of the system, we multiply Equation (72) by the measurement bandwidth f_c, take the square root, and divide by the EF voltage gain from Equation (66) and get [4]

$$|E|_n = \frac{\sqrt{\frac{\bar{v}_n^2}{\Delta f} f_c}}{\frac{d\bar{v}_s}{d|\vec{E}|}}. \quad (73)$$

3.9 Experimental setup of EFM

The experimental setup of the EFM (Figure 24) is very similar to the Electrometer shown in (Figure 21). One difference is that the test voltage is connected to a source electrode a known distance, g, above the EFM. The test voltage induces an electric field equal to v_t/g and perpendicular to the DOT. Data collection is done in the exact same way as the EFS. Test voltages were supplied to the test capacitor in a step pattern.

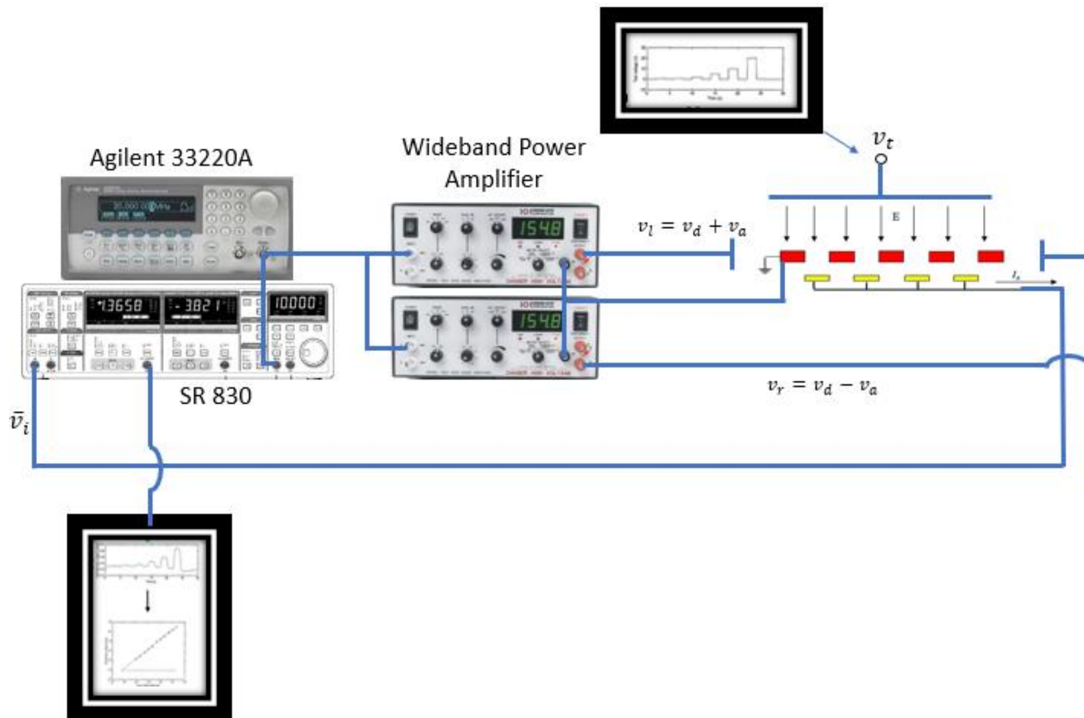

Figure 24. Electrical setup for testing the EFM.

Like the electrometer, the device was placed in a ceramic package and wire bonded to external connections. A brass lid topped the package and is used as the source electrode. Glass spacers prevent charging of the ceramic package, and everything is held together by electric tape. The package was also placed in a Faraday cage for this experiment.

3.10 Summary

This chapter presented the theoretical models of the device modes based on design dimensions. Also, test setups were thoroughly discussed. There are a lot of noise considerations, both internal and external. The internal noise was characterized and measured. External noise is reduced as much as possible. Chapter four presents the results of these test setups.

IV. Results

4.1 Chapter Overview

Chapter four presents the results of this research. These include simulations and physical data. The next section gives the simulated mechanical, electrometer, and EFM results. Then the section after presents the physical data. Neither an electric field nor charge was detected during experimentation. Instead, an analysis of why no signal was detected is given. Chapter 5 gives an analysis of the results and compares the theory to the simulations and physical data.

4.2 Simulation Results

This section gives the simulated results done in COMSOL and MATLAB. First, a mode analysis was done in COMSOL to find the resonant frequency of the primary mode. Then COMSOL was used to simulate the variable capacitance between two vertically spaced electrodes. Finally, the variable capacitance between a source electrode and a vertical EFM was simulated in COMSOL. We used MATLAB to analyze the results of the simulations.

4.2.1 Mechanical Simulations

For this simulation, we made a simplified CAD model of the structure in **Error! Reference source not found.**. Then we used it in COMSOL to simulate the primary mode of the DOT. Figure 26 shows the result of the mode analysis. The resulting resonant frequency was 16499 Hz. This value agrees with the theoretical given in Table 3.

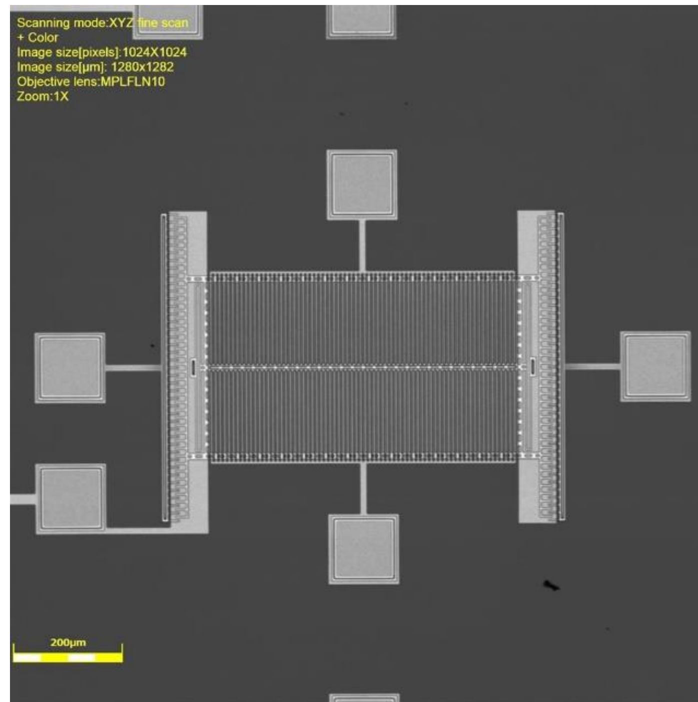

Figure 25. Image of the device under test.

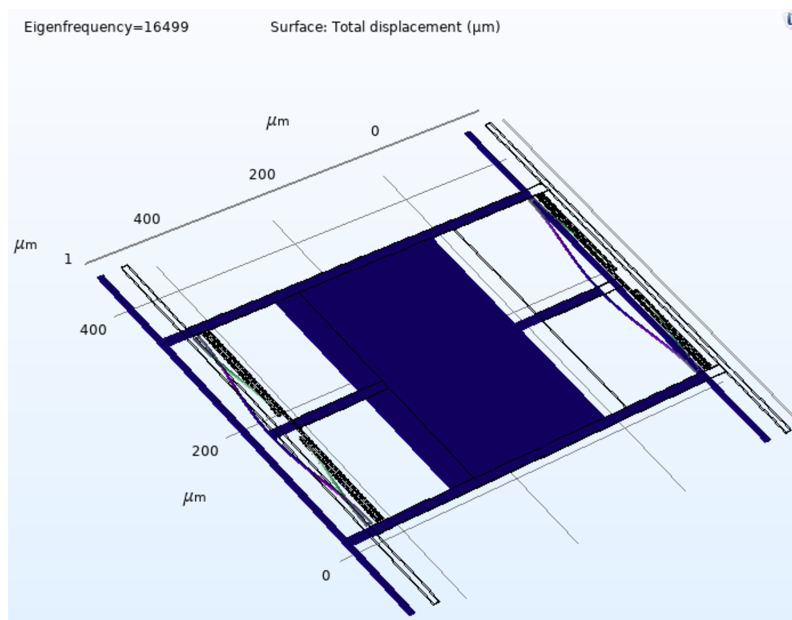

Figure 26. The primary mode of the DOT with a resonant frequency of 16.5 kHz.

4.2.2 Electrometer Simulations

Simulations were done in COMSOL to characterize the capacitance between vertically transverse electrodes. Figure 27 (a) and (b) show a cross section of a simple case simulation consisting of five top electrodes and four bottom ones. The bottom electrodes are all electrically connected with a potential of one volt, and the middle top electrode (indicated by the arrow) is electrically isolated from all the others with a potential of zero. This was done in order to simulate the capacitance of a single electrode. We multiplied the result by n to simulate the effect of n electrodes.

The top electrodes had a sinusoidal displacement with an amplitude of four microns. Figure 27 (c) shows the time-dependent capacitance between the single top electrode and the bottom ones. The peak capacitance is around 2.45 fC, and the trough is 2.15 fC. Ideally, if there were no fringe capacitance, the trough would be equal to the static capacitance. To get a better picture of the effect of the fringing capacitance, the ideal capacitance and the static capacitance were subtracted from the total in MATLAB (results are shown in Figure 27 (d)). It Appears that the fringing capacitance creates a scalar capacitance of the ideal with an opposite sign. This is not good, because it induces a voltage signal that partially jams the one we are interested in.

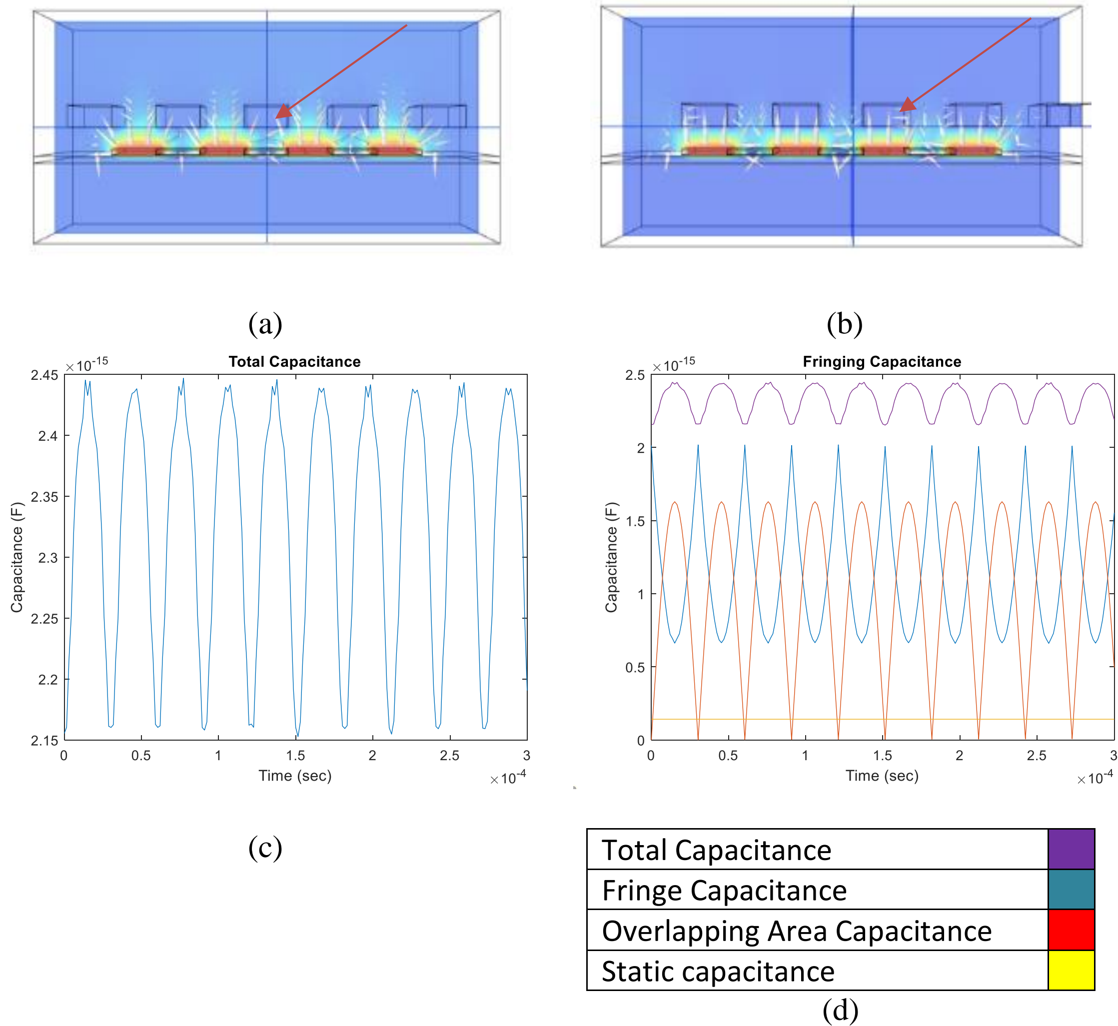

Figure 27. (a) shows the structure created in COMSOL for the simulation with zero displacement. (b) shows the same structure that was displaced 4 microns. (c) shows the time-depended capacitance between the electrode indicated by the arrow and the red electrodes. Warm colors represent areas with higher voltage and cool colors lower voltage.

4.2.3 E-Field Simulations

The same structure of Figure 27 was used to simulate the EFM mode of the device. The variable capacitance between one of the 100 µm long bottom electrodes and a 100 by 200

μm source electrode, 7 μm above, was simulated and is shown in Figure 28. The simulated capacitance is much smaller than the expected capacitance (shown in Figure 29). The expected value has a peak capacitance of 0.5 fC while the simulated peak capacitance is only 0.0634 fC. The difference is due to partial shielding by the grounded shutters. Figure 30 shows how most of the electric field lines do not make it through the shutters; rather they are absorbed by them. This is an effect that was unintended. It would be better to have a larger variance in capacitance because it would create a more sensitive device. The partial shielding minimizes the overall variance.

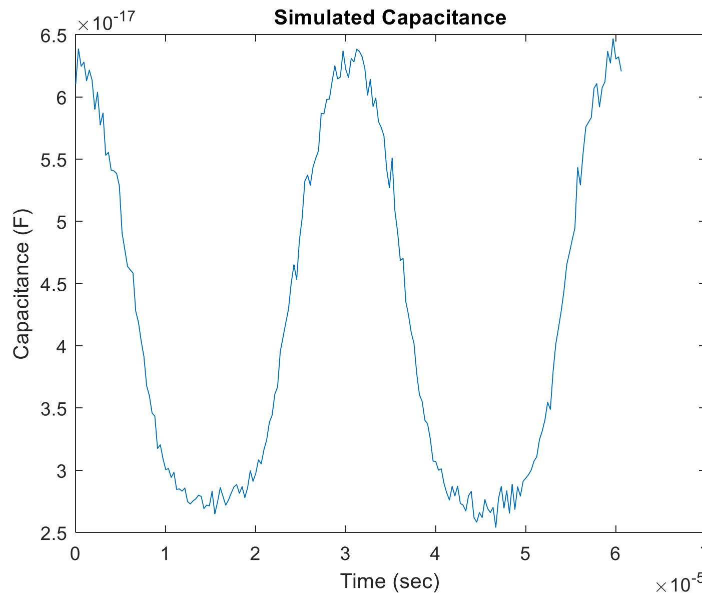

Figure 28. The simulated capacitance between one sense finger and an e-field emitting source electrode.

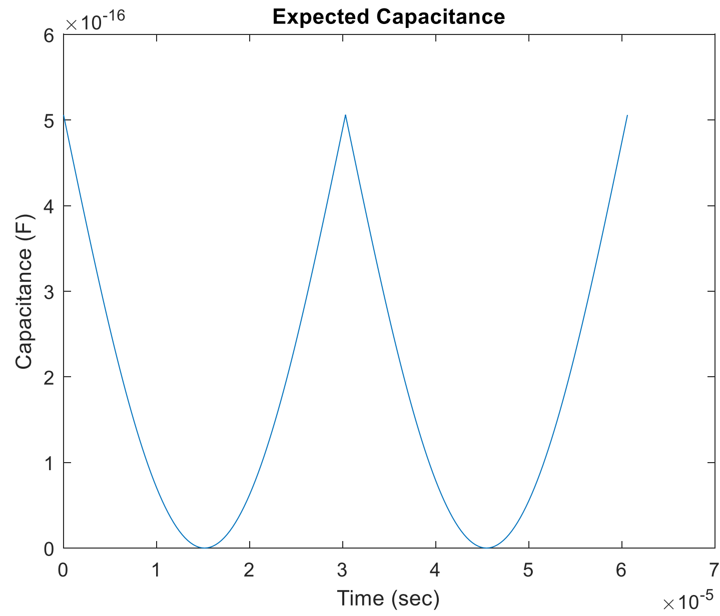

Figure 29. Expected capacitance value for simulation.

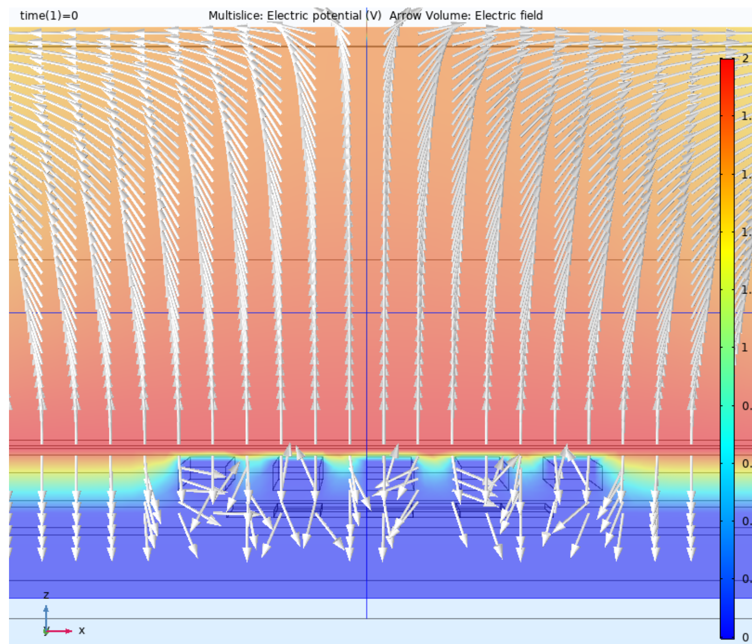

Figure 30. The result of the COMSOL simulation showing electrostatic field lines emitting from the source electrode.

4.3 Electromechanical Results

As discussed in Section 3.3, the dimensions of the device were measured with a 3D microscope. The results of those measurements are shown in Table 4.1. The resonating electrodes were not flat as initially intended. Instead, they had a step height structure shown in Figure 31. This defect does not affect the electric field measurements of the sensor; however, it does affect the electrometer charge measurements. Another defect is that the alignment of the second polysilicon layer was not directly centered over the first, creating an initial overlap of the sense and resonating electrodes. A third defect was that the resonating electrodes were not as wide as designed. The effects of all of these defects are analyzed in the next chapter.

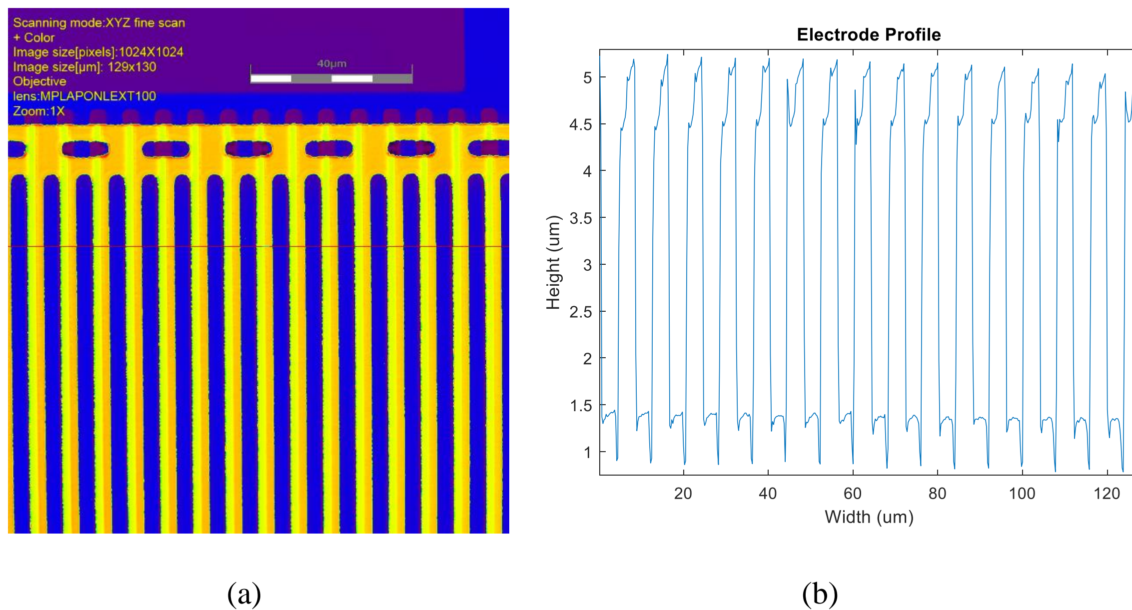

(a) (b)

Figure 31. (a) is a 3D microscope image of the device showing unlevel top electrodes and (b) is a 2d cross section of (a).

Another defect was the width of the beam suspensions. They were 0.5 microns smaller than they were designed to be, which decreases the spring constant as well as the resonant frequency.

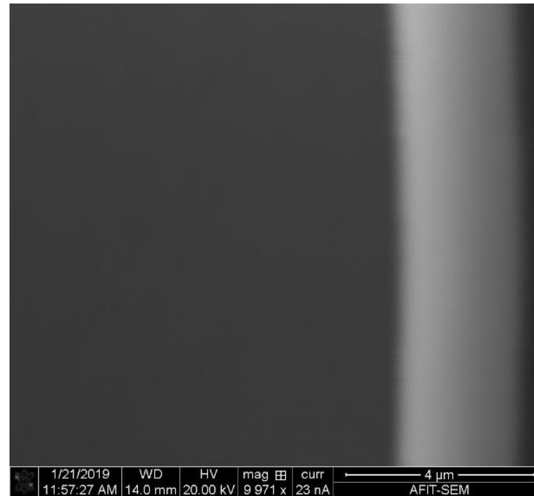

Figure 32. SEM image of the beam suspension. The beam width is shown to be around 2.5 microns.

4.3.1 Mechanical Measurements

The technique discussed in Chapters Two and Three for measuring the mechanical frequency response did not produce a strong enough signal for analysis. This was because the ground electrode was not placed symmetrically even between the two drive combs, so the feed-through noise was not canceled out. Instead, another technique had to be used to measure the frequency response of the DOT.

To produce a detectable signal, the sense electrodes had to be used as a capacitive pick-off. This is a conventional technique used in MEMS resonators for measuring the frequency response [9]. Figure 33 shows the setup for this measurement. It is similar to the setup in Figure 18 except a current preamplifier is used. The input to the preamplifier is a

transimpedance amplifier that converts the sense current into a voltage and applies a bias voltage, V_s, to the sense node. Then the voltage signal is amplified and detected by the lock-in amplifier. Similar to the discussion in Section 2.6.1, a periodic change in capacitance, C_s, between the grounded shutter and sense electrodes induces a periodic change in charge, Q_s, based on the relation

$$Q_s(t) = C_s(t)V_s. \tag{74}$$

The time-varying charge is measured as a current

$$I_s = \frac{dQ_s}{dt} = V_s\frac{dC_s}{dt} = V_s\frac{dC_s}{dx}\frac{dx}{dt} = V_s\frac{dC_s}{dx}\dot{x} \tag{75}$$

where $\dot{x}$ is the velocity of the shutter. It can be seen, from the geometry of the device, that the capacitance between the sense electrodes and the shutter will vary at twice the frequency of the displacement. Therefore, a lock-in amplifier was used to measure the $2f$ component of the signal, where f is the frequency used to actuate the shutter. The signal amplitude is directly proportional to the resonator's amplitude of motion.

Figure 34 (a) shows the measured frequency response of the DOT. The resonant frequency of the device was 12.62 kHz with a quality factor equal to 22.54. Assuming that the mass of the structure is equal to the theoretical value, the remaining motional coefficients were calculated and are shown in Table 4.

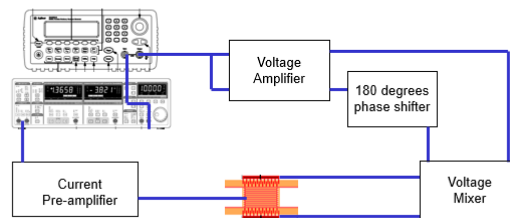

Figure 33. Frequency response measurement setup.

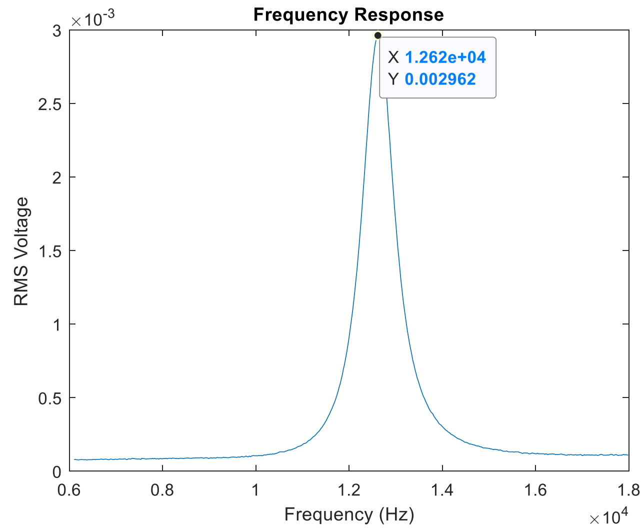

(a)

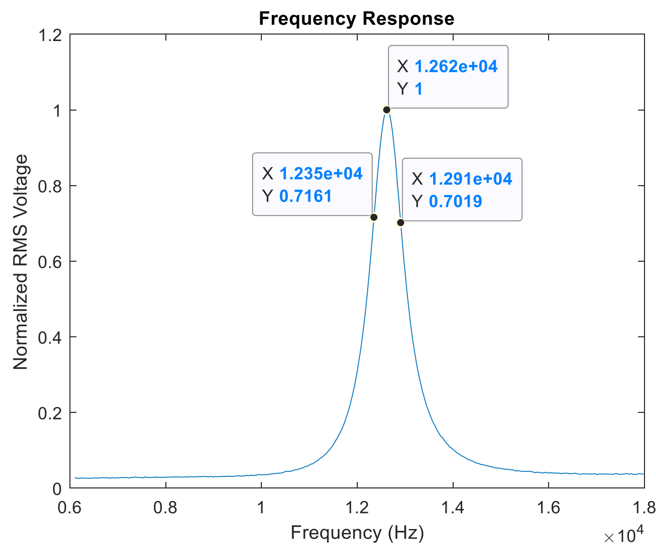

(b)

Figure 34. The figure above shows the frequency response of the resonator. (a) shows the RMS voltage measured by the lock-in amplifier with respect to frequency (with a gain of 500 thousand). (b) shows the same response normalized to an amplitude of 1. Curser marks highlight the peak of the response at the resonant frequency and the half -3db frequencies. The -3db frequencies are used to calculate the quality factor.

Table 4. Mechanical Values

Parameter	Calculated value based on design dimensions	Actual Value
Actuation DC Voltage (V)	80	80
Actuation ACVoltage (V)	7	8
Sense Voltage V_s (V)	2.5	2.5
Signal Amplification	500 k	500 k
Mechanical part film thickness (µm)	2	2
Suspension beam length l_s (µm)	135	135
Suspension beam width w_s (µm)	3	2.5
Spring constant (folded beam in N/m)	6.13	3.55
Structure mass (µg)	0.56	0.56
Resonant Frequency (kHz)	16.65	12.62
Drive comb gap g_d (µm)	3	3.5
Number of drive combs (each side) n_d	40	40
dC/dx of drive combs (F/m)	9.44E-10	7.55E-10
Sense electrode gap g (µm)	2	1.4 (Average)
Resonating electrode length l_c (µm)	150	150
Resonating electrode width w_c (µm)	4	3.33
Resonating electrode overlap ol (µm)	0	1
Number of sense electrodes n_c (each side)	70	70
Displacement amplitude $\hat{x}$ (µm)	4	3.3E-6
Damping Coefficient (N·s/m)	1.19E-6	1.98E-6
Quality Factor	51.28	22.54
Maximum Capacitance C_{max} (between sense electrodes and mechanical mass in pF)	0.186	0.22
Static capacitance C_0 (between sense electrodes and mechanical mass in pF)	0.01	0.01
Change in fringing capacitance C_f (between sense electrodes and mechanical mass in pF)	-0.155	(Not measured)
Change in total capacitance ΔC (between sense electrodes and mechanical mass in pF)	0.033	(Not Measured)

4.4 Electrometer Results

Several attempts were made to measure a charge with our system with no success. It was determined that the input impedance of our electrometer was too low. The required input impedance for an electrometer is greater than 1 GΩ [4]; ours was around 800 K. Any charge that was at the input of the device was quickly swept away across the low resistance. Essentially, the input resistance acted like a pull-down resistor that forced the input node to have zero potential. A short somewhere in the system most likely caused the low resistance.

4.5 Electric Field Sensor Results

This experiment also resulted in no signal detected. An electric field was emitted from a brass electrode, 500 µm above the device. Voltages up to 200 V were supplied to the source electrode relative to the device structure, and still, no signal was detected. Using the simulated results and the theory developed in Chapter three, the device induced a current signal at the second harmonic with an amplitude of 8.77E-10 A. Then, that current was amplified by 500,000 with a current pre-amplifier and measured with the lock-in amplifier. If the simulations are accurate, the signal was 3.1E-04 V_{rms}. The noise floor of the system was 1.07E-04 V_{rms}. We did not detect a signal because of two possibilities. One, the theoretical resolution is most likely not the actual, so the electric field was not large enough to produce a signal. Two, there may have been an alternate current path to ground somewhere in the system.

4.6 Conclusion

This chapter presented the simulated and actual results of this research. The simulated and actual resonant frequencies differed by almost 4 Hz. Chapter 5 discusses why that is. No signal was detected for either mode of the device. The most likely reason why the electrometer did not detect a charge is because the input impedance was too low. The EFM did not detect an electric field for possibly two reasons: one, the theoretical resolution is most likely not the actual; and two, there may have been an alternate current path to ground. Still, we were able to use the simulation results to make predictions on the performance of the device. This is done in the next chapter.

V. Analysis

5.1 Chapter Overview

The previous chapter presented the simulation results as well as the experimental results. This chapter goes in depth with analysis. The only physical data analyzed was the mechanical results of Section 4.3. We used that data to justify the simulation results. Then the simulations are used to predict the responsivity for both modes of the device (electrometer and EFM). Finally, we compared the theory developed in Chapter Three to these predictions. Section 5.2 analyzes the mechanical data collected. The next two sections analyze what can be inferred from our electrometer and EFM simulations.

5.2 Mechanical Results Analysis

In this section, the data collected in Section 4.3 is analyzed. First, the frequency response of the actual device is compared to the simulated results and the theory. Then the device deformations are analyzed to predict the effect on the responsivity of the two sensor modes. Then we compare the voltage signal output to the variable capacitance simulation of Section 4.2.2.

5.2.1 Resonant Frequency

The mode analysis in COMSOL nearly predicted the exact resonant frequency as the theoretical (Section 4.2.1). However, the actual device had a smaller resonant frequency. The theoretical resonant frequency is 16.65 kHz while the actual was measured at 12.62 kHz (Section 4.3.1). The difference is from a reduction in the suspension beam width. The suspension beams were designed to be 3 μm wide. Scanning electron microscope measurements show that the beam widths are only 2.5 μm (Figure 32). Using Equation

(41) and (32), the theoretical resonant frequency of the device with a 2.5 μm suspension beam width is 12.669 kHz, much closer to the actual measurement.

5.2.2 Effects of Defects

As mentioned in Chapter 4, the top electrodes were not completely flat. Rather they had a geometry similar to the one in Figure 35. They have a u-shape and are thinner than designed. The overlapping area capacitance was simulated in MATLAB. The results were compared to the ideal case for both the electrometer mode and the EFM mode.

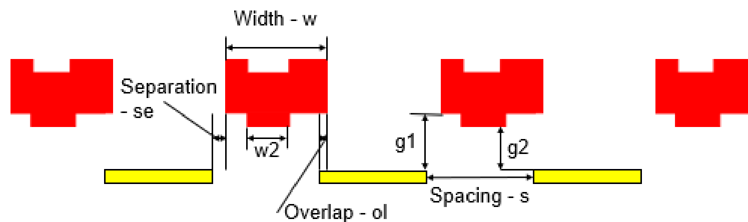

Figure 35. Illustration of defects.

While in electrometer mode, the capacitance of interest is between the top electrodes and the bottom electrodes. Simulations were done in MATLAB characterizing one electrode with a length of 200 microns. The results are shown in Figure 36. We transformed the capacitances into the frequency domain with a fast Fourier transform and recorded the second harmonic amplitudes of each. The amplitude of the real case is smaller than the ideal. So, the sensitivity of the device will be lower than the ideal case. However, they do not differ by much.

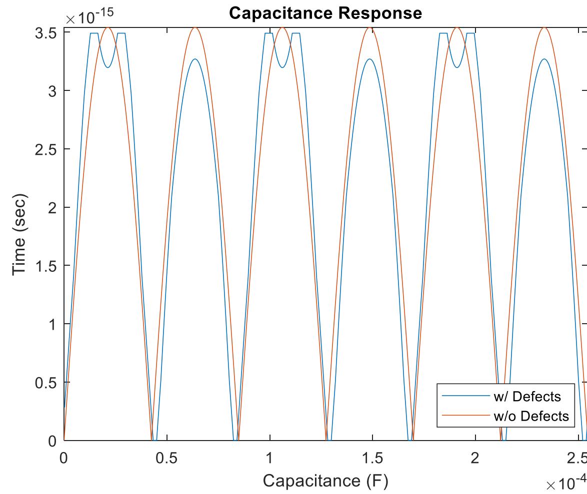

(a)

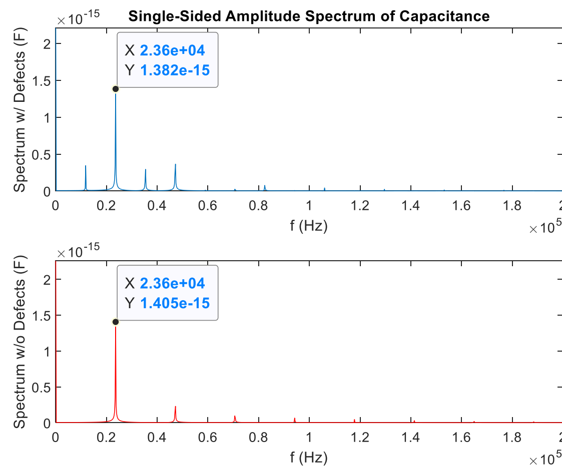

(b)

Figure 36. (a) shows the time domain capacitance between one top electrode and one bottom. (b) shows the capacitance in the frequency domain. Results are shown for both the ideal electrode and deformed.

In the case of the EFM, the capacitance of interest is between the bottom electrodes and a source electrode far above the device. The unlevel top electrodes do not affect the EFM measurements. However, their smaller widths do. The electric field emitting electrode was simulated 600 microns over the device. The results comparing the ideal capacitance to the capacitance with defects is shown in Figure 37. The frequency domain

transformation shows that the defects do have a negative effect on the performance of the device. However, the effect is not very significant.

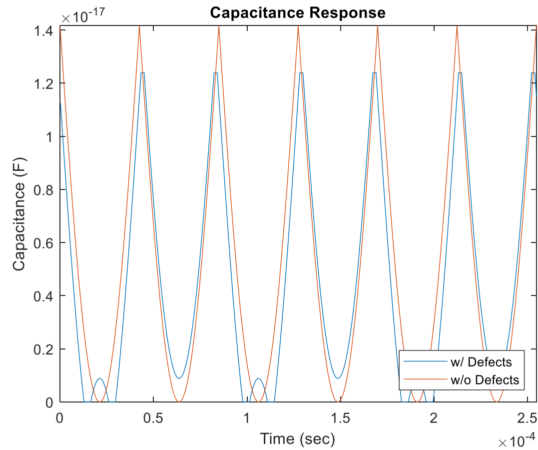

(a)

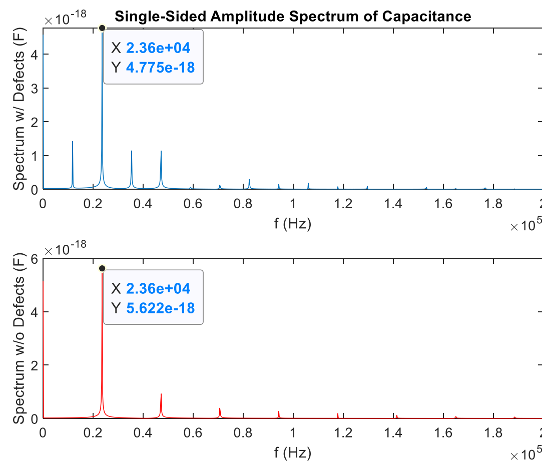

(b)

Figure 37. (a) shows the time domain capacitance between one bottom electrode and a source electrode 600 microns away. (b) shows the capacitance in the frequency domain. Results are shown for both the ideal electrode and deformed.

5.2.3 Mechanical Voltage Signal at Resonance Compared to Simulations

Section 4.2.2 presented the COMSOL simulation of the capacitance between a single top electrode and an array of bottom electrodes, all with lengths of 100 micrometers. The simulated gap between the two sets of electrodes was two micrometers. We used the

simulation to estimate the capacitance between 70 vertically spaced electrodes with lengths of 150 micrometers and a vertical gap of 1.4 micrometers. The 1.4-micrometer gap is near the average gap distance between the two sets of electrodes. Our MATLAB model utilized this estimation to simulate the current output of our device at resonance and with a sense voltage of 2.5 volts. The MATLAB simulation imitates the actual data collected and presented in Section 4.3. As mentioned before, a current preamplifier converted the signal into an equivalent voltage with amplification of 500 thousand. Then a lock-in amplifier measured the RMS voltage at the second harmonic of the signal output. Figure 38 shows the MATLAB simulation of the output signal.

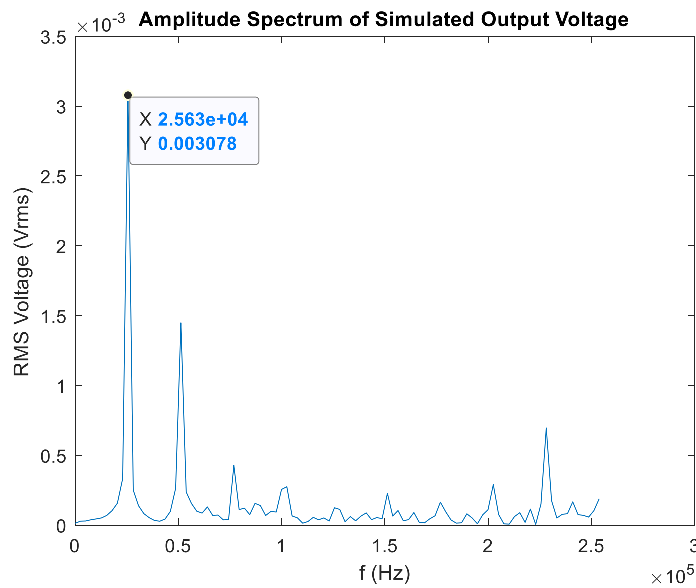

Figure 38. This figure shows the amplitude spectrum of the simulated voltage signal at resonance. A voltage of 2.5 V chosen as the sense voltage.

The second harmonic component of the signal has an amplitude of 3.078 mV_{rms}. The amplitude is comparable to the actual value, which is 2.962 mV_{rms} (Figure 34).

5.3 Electrometer Results Analysis

Unfortunately, we were unable to detect a charge with our device. The input impedance wasn't high enough to hold a charge. Still, we can use the variable capacitance simulations to predict the responsivity of our device. This is done in the next section. The following section compares the theory developed to the simulated results.

5.3.1 Simulated Electrometer Charge Conversion Gain

Since the capacitance simulation between the top and bottom electrodes agrees with the actual results, we can use them to predict the charge resolution of our device. This prediction assumes that our device has a high input impedance and can hold a charge long enough to measure.

The responsivity is defined as the increase in voltage amplitude output per charge input. Figure 39 shows the Spectral density of the response. The simulation was made assuming a parasitic capacitance of 155 pC. We are only interested in the 2.55 kHz component of the response since that is the frequency measured by the lock-in amplifier. The predicted response of our device is $8.608 \cdot 10^5$ V/C.

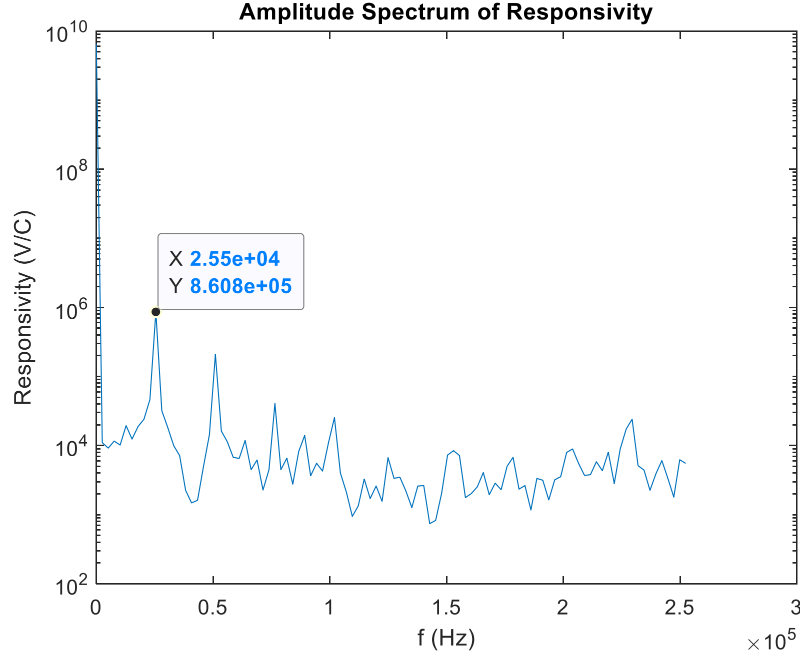

Figure 39. The figure above shows the amplitude spectrum of the simulated electrometer responsivity.

5.3.2 Electrometer Theory Compared to Simulations

Including the method above, there are two other ways to approximate the responsivity of the device. One is by using MATLAB to solve the integral

$$\frac{2}{\pi(C_{max}+\Delta C_f)}\int_0^{\pi}\frac{\cos(2\tau)\,d\tau}{\sin(\tau)+\alpha}. \tag{76}$$

MATLAB solves the integral using global adaptive quadrature and default error tolerances. Another way to solve the integral is by approximating it as

$$\frac{2}{\pi(C_{max}+\Delta C_f)}\left(2\alpha\pi-4-\frac{(4\alpha^2-2)\tan^{-1}(\sqrt{\alpha^2-1})}{\sqrt{\alpha^2-1}}\right). \tag{77}$$

In Equations (76) and (77), α is equal to $\frac{C_{p0}+C_{f0}}{C_{\max}+\Delta C_f}$, the total static capacitance divided by the change in capacitance (see Section 3.4).

To test the concordance between the three approximations, we did a 2-to-the-4 factorial analysis. Meaning, we chose four controllable variables: the number of sense fingers, length of each finger, the gap between sense fingers and the resonator, and the parasitic capacitance; and chose two levels for each. The levels were chosen at the extreme low and high values. The aliases used are 1 and 2 and are assigned as shown in Table 5.

Table 5. Alias Structure for Factorial Analysis of Electrometer Responsivity Prediction

Alias	Number of Fingers	Length (μm)	Gap (μm)	Cp (nF)
1	1	10	0.5	6
2	1000	1000	3	1000

The result of the analysis is shown in Table 6. The values of Responsivity 1-3 correspond to the three methods of approximation: COMSOL simulation, MATLAB solution to Equation (76), and Equation (77). Also listed is the Alpha value for each combination of factors ($\alpha = \frac{C_{p0}+C_{f0}}{C_{\max}+\Delta C_f}$).

Table 6. 2^4 Factorial Analysis for Electrometer Responsivity Prediction

Number of Fingers	Length	Gap	Cp	Responsivity 1	Responsivity 2	Responsivity 3	Alpha
1	1	1	1	1.65E+06	1.45E+06	1.51E+06	4.88E+4
1	1	1	2	5.94E+01	5.22E+01	-3.86E+07	8.13E+6
1	1	2	1	2.75E+05	2.42E+05	0	2.93E+5
1	1	2	2	9.89E+00	8.70E+00	1.85E+09	4.88E+7
1	2	1	1	1.60E+08	1.40E+08	1.40E+08	4.95E+2
1	2	1	2	5.93E+03	5.22E+03	3.01E+03	8.13E+4
1	2	2	1	2.73E+07	2.40E+07	2.40E+07	2.93E+3
1	2	2	2	9.89E+02	8.70E+02	0	4.88E+5
2	1	1	1	1.14E+09	9.98E+08	9.98E+08	5.82E+1
2	1	1	2	5.92E+04	5.21E+04	5.21E+04	8.14E+3
2	1	2	1	2.57E+08	2.26E+08	2.26E+08	3.02E+2
2	1	2	2	9.89E+03	8.69E+03	9.04E+03	4.88E+4
2	2	1	1	5.89E+08	5.14E+08	5.14E+08	7.62E+0
2	2	1	2	4.95E+06	4.35E+06	4.35E+06	8.85E+1
2	2	2	1	2.09E+09	1.83E+09	1.83E+09	1.01E+1
2	2	2	2	9.59E+05	8.43E+05	8.43E+05	4.95E+2

To test for concordance, we used Lin's concordance correlation coefficient (ccc) [31]. Which, for two sets of corresponding data, is divined as

$$\hat{\rho}_c = \frac{2s_{xy}}{s_x^2 + s_y^2 + (\bar{x} - \bar{y})^2} \tag{78}$$

Where s^2_x and s^2_y are the variances of the two datasets, $\bar{x}$ and $\bar{y}$ are the means for each, and s_{xy} is the covariance between the two sets. The coefficient can range between -1 and 1. Values of ±1 denote perfect concordance and discordance; a value of zero denotes its complete absence [31]. The ccc between responsivity 1 and 2 is 0.989. This tells us that the two data sets are nearly the same.

In Table 6, Responsivity 3 has some outlier values. These appear to correspond with large alpha values. To investigate, the integral part of Equation (76) was plotted with respect to alpha. Figure 40 gives the result of the plot. The blue line shows the MATLAB

numeric solution to the integral, and the red line shows the solution of the integral when approximated with Equation (77). Equation (77) becomes unstable with large alpha values. This occurrence is of no great concern while designing these devices because a large alpha value also means low responsivity. These devices are designed with a large responsivity.

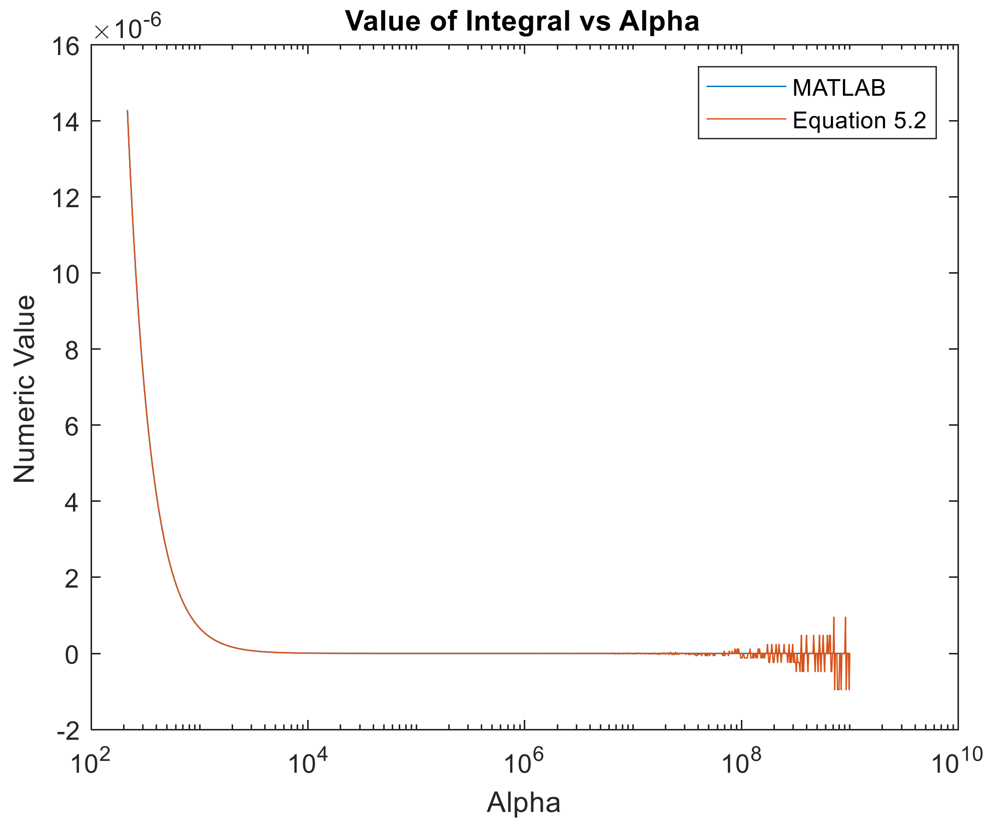

Figure 40. Solution to the integral in Equation (76) with respect to the alpha value. The blue line shows the MATLAB numeric solution to the integral, and the red line shows the solution of the integral when approximated with Equation (77).

If the outliers, corresponding to alpha values greater than 5E4, are removed from the data set, the ccc between responsivity 1 and 3 is 0.988, Which is close to perfect concordance.

5.4 EFM Results Analysis

Unlike the electrometer, the mechanical data does not relate to the capacitance of interest for the EFM. Instead, we are interested in the capacitance between the sense node and a source electrode far above the device. This capacitance was never recorded. All we have to go off of are the simulated results. There is no physical data to disprove or prove the simulations. But since the capacitance simulations for the electrometer agreed with the actual results, then the EFM simulations are most likely accurate. We used the simulations to predict the responsivity of our device and compared them to the theory.

5.4.1 Simulated EFM Responsivity

The capacitance simulations of Section 4.2.3 and the theory developed in Chapter 3 were both used to predict the responsivity of our device. The simulation shows the capacitance of one electrode 100 μm long and a source electrode 7μm away. The results were multiplied by the number of sense fingers, and then they were multiplied by the ratio of the actual length to the simulated length, and they were divided by the ratio of actual gap to the simulated gap. These multiplications gave an estimate of the actual capacitance. Then we followed the theory developed in Chapter three to estimate the responsivity of the device. The resulting amplitude spectrum is shown in Figure 5.6. The second harmonic portion of the spectrum has an amplitude of 2.189E-15. This means that for every V/m increase in electric field, the EFM signal will increase 2.189E-15 amps. Given the noise floor at 3.026E-10 V, the device would theoretically be able to detect a minimum electric field equal to 138.25 kV/m.

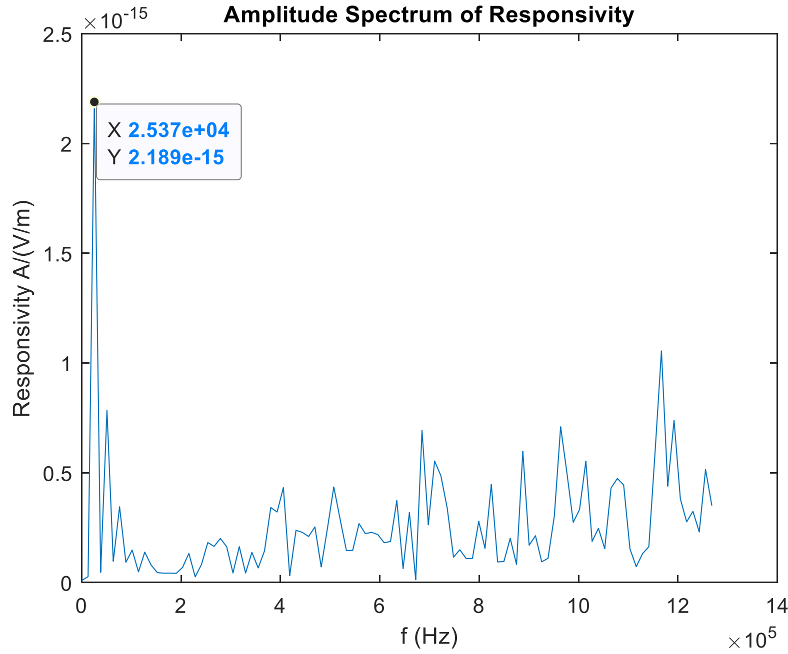

Figure 41. The figure above gives the simulated results for responsivity of the EFM mode.

5.4.2 EFM Theory Compared to Simulations

The theory did not consider the partial shielding of the top electrodes while stationary. This lowered the overall change in capacitance at the sense node and decreased the responsivity. The responsivity model was updated to account for this change and is denoted as

$$\frac{d\overline{v}_s}{d|E|} = \Delta C f g \frac{8\sqrt{2}}{3} A_g. \tag{79}$$

where ΔC is the maximum minus the minimum capacitance of the variable capacitor, f is the resonant frequency, and g is the distance between the source voltage and the sense electrodes.

To validate the equation, a two-factor simulation was done. We chose two settings of the controllable factors: the number of sense electrodes and the length of each. The factors were set at 1 and 1000 for the number of fingers, and 10 μm and 1000 μm for the length. The result of the factor experiment is shown in Table 7. Responsivity 1 gives the MATLAB estimate, and responsivity 2 gives the estimates calculated from Equation (79). The two sets of numbers have a Lin's concordance correlation coefficient of 0.98. This means the two sets of numbers are statistically similar.

Table 7. 2^2 Factorial Analysis for EFM Responsivity Prediction

Number of Fingers	Length	Responsivity 1	Responsivity 2
1	1	2.10E-18	1.77E-18
1	2	2.10E-16	1.77E-16
2	1	2.10E-15	1.77E-15
2	2	2.10E-13	1.77E-13

5.5 Chapter Summary

This chapter analyzed the results of chapter four. The theory, simulations, and the data collected for the frequency response all agreed. This gave us the confidence to use the simulations to predict the responsivity of the device in electrometer mode. The responsivity was estimated to be $8.608 \cdot 10^5$ V/C. The theoretical model, for the responsivity, shows good comparison with the simulations. In the case of the EFM simulations, we had no physical data to verify those. However, we still used them to estimate the responsivity while in EFM mode. We estimated a responsivity of 2.189E-15 A/(V/m). The theoretical model for this also compares well to the simulations.

VI. Conclusion and Recommendations

6.1 Chapter Overview

This research gave the first iteration of a dual Vertical electrometer and EFM. Theoretical models were developed in Chapter three, simulations and results were given in Chapter four, and a thorough analysis was done in Chapter Five. This chapter makes ultimate conclusions for this iteration, gives recommendations for future iterations, and suggests future research.

6.2 Conclusion

For the first time, a dual electrometer and EFM device was developed. Also, for the first time, a vertical electrometer was developed, and a unique geometry for modulating an electric field is demonstrated. Both modes failed to detect a signal. However, much can be inferred from this iteration of devices. The next two sections conclude the discoveries for each mode.

6.2.1 Electrometer

The electrometer in this research was not able to measure charge. The input impedance was too low, around 800 kΩ. Still, we were able to extract useful information from the frequency response data.

The frequency response signal was generated by the variable capacitance of the vertically spaced electrodes. The peak output voltage occurred at 12.62 kHz with a measured voltage amplitude of 2.962 mV_{rms}. The simulated output voltage was 3.078 mV_{rms}. The two amplitudes are comparable and give us the confidence to use the simulations for estimating the electrometer responsivity. With a parasitic capacitance of

155 pF the predicted responsivity of the electrometer is $8.608 \cdot 10^5$ V/C. This tells us that for every Coulomb of charge on the sense electrode, there will be an increase of 861 kV in the output signal peak voltage.

The response of the electrometer is comparable to the MEMS electrometer created by Lee *et al.* [3]. They tested laterally spaced electrometers. One of their electrometers had a sense capacitance equal to 0.372 pF; which is close to the peak capacitance of 0.3556 pF for our electrometer (although, theirs was much bigger and more than twice the surface area). Their device had a responsivity of $1.96 \cdot 10^6$ V/C, slightly greater than ours. They also used lower drive voltages. They had a DC voltage of 30 V and AC voltage of 10 volts peak compared to our 80 and 8 respectively. However, their device had 100 drive comb fingers on each side, while ours only had 40. Given 100 drive comb fingers with minimally added mass, our devices could operate at 30V DC and 10V AC and still obtain the same displacement, close to 3.3 μm.

The main advantage of the vertical electrometers over the lateral is that they are lighter and create less damped systems. Our electrometer only weighs 0.56 μg and had a damping coefficient of 1.98 μN·s/m. Lee's weighed 4.8 μg with a damping coefficient of 31 μN·s/m. Also, vertical electrometers can obtain nearly the same responsivity with a fraction of the total surface area when compared to lateral electrometers. This is advantageous in the microelectronics industry because twice as many devices can be made per fabrication run.

There are positive and negative aspects for both types of devices. In general, vertical electrometers are less damped weigh less and take up less space. However, they have larger displacements and still require large actuation voltages. The advantages of lateral electrometers are they do not suffer from stiction, they have small displacements, the

fringing fields are minimal, and they do not add as much unnecessary static capacitance. The disadvantages are they are large, heavily damped, and they have a limit on how far they can displace.

6.2.2 EFM

This research developed a unique way to detect an electric field. Most other MEMS electrometers utilize differential sensing to reduce feedthrough noise. This devise reduced feedthrough utilizing harmonic sensing. We designed the device to have nonlinearities that separated the sense signal from the feedthrough noise. This research developed a theoretical model for the output signal and confirmed it with simulations. Despite constant attempts, no electric field data was recorded. The failure is most likely due to the sensitivity of the device. Another likely reason could have been that there was an alternant current path to ground reducing the signal. Still, we were able to use the simulation results to predict the responsivity of the device. Based on the simulations, the responsivity is 2.189 pA/kV m^{-1}.

A similar device, created by Peng *et al.* [32], was also created using PolyMUMPs. Their device was a vertical EFM that utilized differential sensing. They were able to achieve a responsivity of 19.5 pA/kV m^{-1} with an overlapping area of 2.24E-7 m^2. The device of this research had an overlapping area equal to 4.2E-8 m^2. The ratio of responsivity between their device and ours is 8.9, and the ratio between the two areas is 5.33. Comparing these two numbers tells us that their device is more efficient than ours.

The advantage of the device of this research is that it utilizes harmonic sensing. Harmonic sensing has a greater potential to create less noise in a system. A disadvantage

is that our device was less efficient than others, meaning it created less variability in capacitance per square area when compared to other devices.

6.3 Recommendations

- Breach the nitride layer and form a contact with the substrate – The substrate of the device needs to be grounded. Otherwise, it will build up a charge and create a potential between itself and the grounded shutter. The voltage difference will eventually get large enough to pull the shutter into the substrate and cause stiction. After that, the only way to un-stick the shutter is by moving it with a probe tip. The devices in this research did not have a breached nitride layer, so the only way to ground the substrate in the package was by soldering it to the package base. However, if the nitride layer was breached and a contact was made to the substrate, then normal nonconductive crystal bond could be used to attach the die to the package, and the substrate can be grounded to one of the pins of the package.
- Place Contacts near the edge of the die – Figure 25 shows the device with contacts placed near it. This was done to reduce parasitic capacitance between the sense node, ground, and the left and right drive combs. Doing this created an issue, however. When wire bonding between the contact and the package pin, the wire would droop and touch the substrate. Then, everything was shorted when the device was tested. To fix this, after every bond, the wire had to be shaped using tweezers so that it wouldn't touch the substrate. But, if the contacts were routed to the edge of the die, then the bonds could be made without risk of touching the substrate (Figure 42).

Figure 42. A depiction of a side contact vs. a center one. The side contact is less likely to form a connection with the edge of the chip.

- Create more dimples in the structure – These devices were plagued with stiction. The devices would get stuck to the substrate, and the only way to get them unstuck was with a probe tip. If more dimples were used, however, then the devices could be un-stuck be simply shaking them. A dimple is depicted in Figure 43. It forms a narrow point beneath the structure so that the dimple, instead of the entire shutter, contacts the substrate reducing the force of stiction.

Figure 43. A depiction of having dimples vs. no dimples.

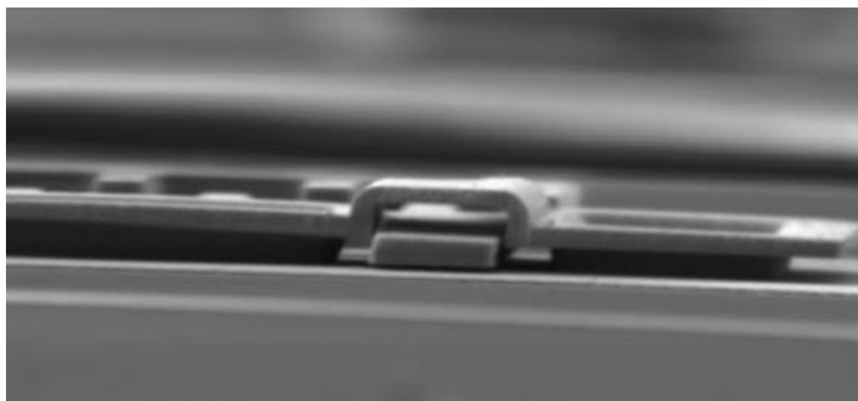

Figure 44. An SEM image showing stiction of the device.

- Ground the restraining pillars/ get rid of them – For this research, we designed restraining pillars that formed over the mechanical polysilicon layer (Figure 45). The pillars were designed to prevent any out-of-plane motion. Just like the ungrounded substrate, the pillars would build-up a charge, pull-in the shutter, and it would become stuck. To prevent this, the restraining pillars would have to be grounded; either to the substrate or through routing to a ground contact. Another alternative is to get rid of the pillars. The suspension beams used for these devices are designed to prevent out of plane motion. The devices with the pillars were not tested. See Appendix 1 for the entire layout of the chip with different designs for the device.

Figure 45. SEM image of pillar used for preventing out of plane motion.

- Line routing with gold – It is always advantageous to line the electrical routing with gold. It lowers the resistance of the routing and generates cleaner signals. Unfortunately, that was not done in this research, but it should be implemented in future iterations.

6.4 Future Work

- Variable fringe capacitor – The electrometer mode was not very sensitive because the fringing capacitance created a negative scaler of the signal of interest, which was the signal induced by the overlapping area capacitance. The fringing capacitance cannot be reduced. But what if a system was created that only utilized fringing capacitance to modulate a charge signal? The system can look like the one in Figure 46. The top electrode will displace and nearly overlap the bottom electrode, so no overlapping area capacitance is implemented into the system. This will create a variable capacitance with a larger delta value.

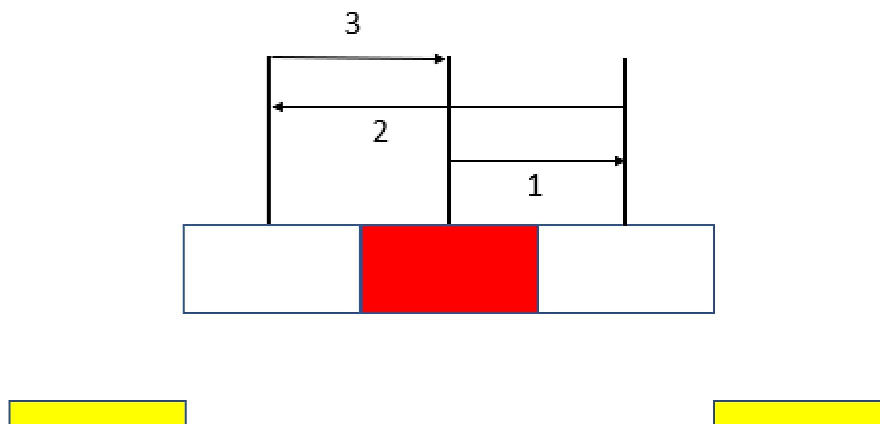

Figure 46. The figure above shows the path of displacement for the grounded electrode in a fringe capacitor. The electrode starts in the center, moves distance 1, then 2, then three, and repeats with a sinusoidal velocity.

- Create a low noise system – We were only able to complete one iteration of this research because of time restraints. In the next iteration, we would create a detection system with less noise. This would require low noise voltage generators, a well calibrated lock-in amplifier, and low noise voltage buffers and other circuit

components. It would also be better to use a circuit board instead of a breadboard. Also, the voltage generator and lock-in amplifier should be operated using battery power to reduce wall power noise. In addition, low noise coaxial cables should be used, and the whole experiment should be placed in a metal box.

- Implement MEMS CMOS fabrication process – External coaxial cables and wires created a large parasitic capacitance in the experiment and greatly limited the sensitivity of the electrometer mode of the device. All of the additional parasitics can be reduced, however, if a voltage buffer was fabricated on-chip with the device. A MEMS first CMOS fabrication process would be perfect for this application. The only parasitics that affect the sensitivity are coupled to the voltage node before the input of the buffer. All of the parasitics after do not limit the sensitivity [33].
- Add a partial backside etch to the fabrication process – The parasitic can be further reduced by adding a partial back side etch to the fabrication process. This etches away all of the grounded silicon substrate beneath the sense electrodes. Without the etch, the highly dialectic silicon nitride creates a high parasitic capacitance between the sense electrodes and the substrate. This etch can be done at the end of the standard PolyMUMPs process. The backside of the die would need to be patterned with photoresist, and then the silicon substrate can be selectively etched away with KOH. Silicon nitride is a natural buffer layer that is not etched by KOH. Etching away the nitride layer beneath the device will also be beneficial by greatly reducing slide film damping.
- Vacuum Packaging – Damping effects can be further reduced by packaging the device inside a vacuum. Several common techniques can be used to do this.

However, implementing surface micromachining, a back-side substrate removal, and vacuum packaging is a difficult task. The easiest way to do that would be to use a flip-chip vacuum packaging technique.

6.5 Chapter Summary

This research developed a MEMS vertical electrometer with an EFM mode. All other MEMS electrometers are lateral electrometers with laterally spaced electrodes. Both types demonstrate comparable performance, but the vertical electrometer does so at a fraction of the size of lateral electrometers. Also, the vertical electrometer can easily have an electric field sensor mode. The electric field sensor did not compare as well to other MEMS electric field sensors. However, the dual nature of this device makes it appealing. The devices can be used in missiles and satellites to monitor charge buildup in electrical components and the atmosphere [11]. They were created using inexpensive materials and common fabrication techniques.

This iteration developed the theory behind the devices and fabricated non-working devices. The electrometer mode did not work because the input impedance was too low to hold a charge. The EFM mode failed to work because the electrical signal was too small. To fix this, simply a larger device needs to be fabricated that can produce a large enough electric field signal. Future iterations should heed to the recommendations in this chapter to create a working device. If so, then the electrostatic sensors can be made cheaper and smaller than common sensors used today.

Appendix

The picture below shows the full 1 cm by 1 cm die layout that was created using PolyMUMPs. The only two working devices on the entire die are circled in red. The large devices on the left may have worked if the pillars were not used.

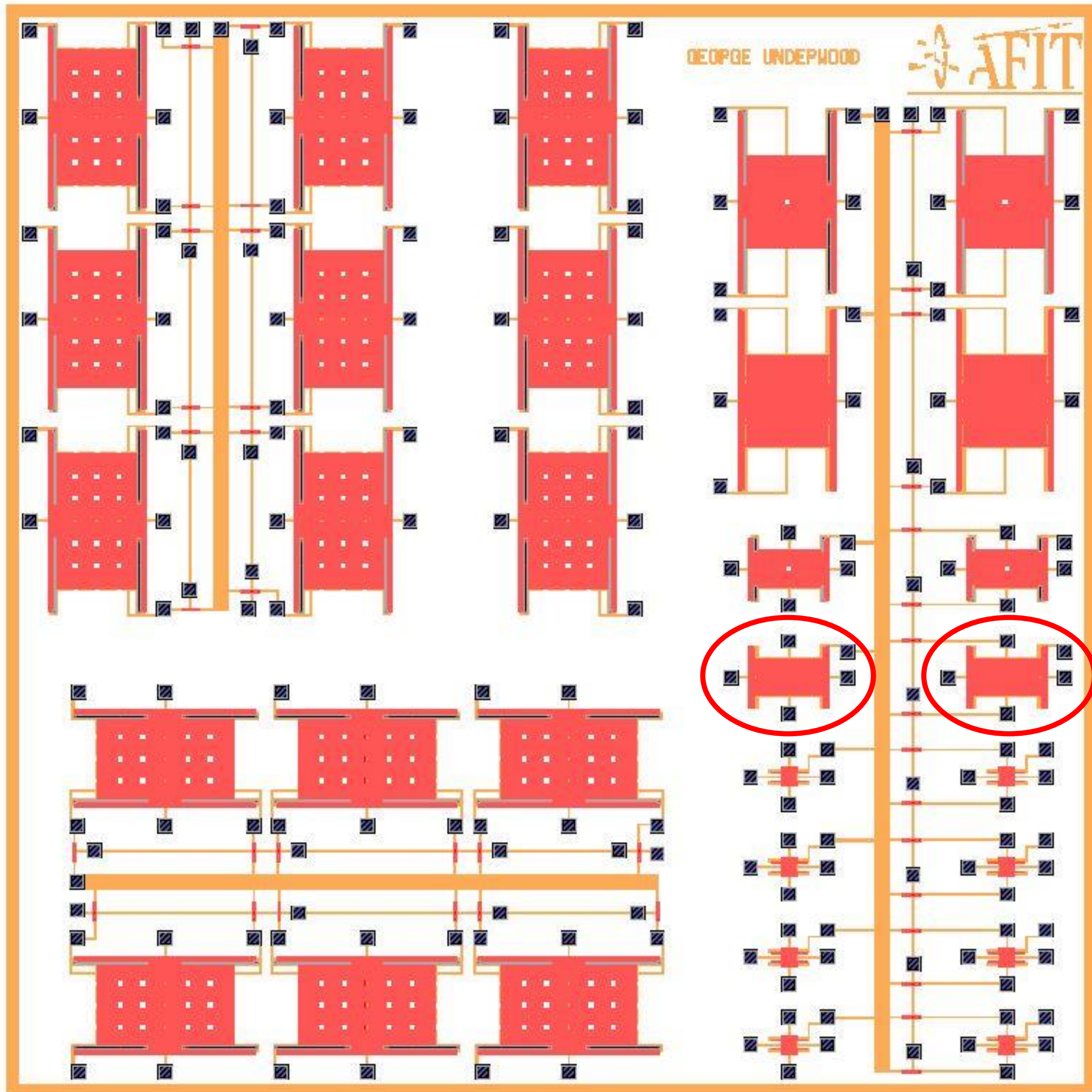

Bibliography

[1] J. Jalil, Y. Zhu, C. Ekanayake, and Y. Ruan, “Sensing of single electrons using micro and nano technologies: A review,” *Nanotechnology*, vol. 28, no. 14, 2017.

[2] P. S. Riehl and K. L. Scott, “Electrostatic Charge and Field Sensors Based on Micromechanical Resonators,” *J. Microelectromechanical Syst.*, vol. 12, no. 5, pp. 577–589, 2003.

[3] J. Lee, Y. Zhu, and A. Seshia, “Room temperature electrometry with SUB-10 electron charge resolution,” *J. Micromechanics Microengineering*, vol. 18, no. 2, 2008.

[4] M. Suazo, “Microfilmed 2003,” 2002.

[5] J. Lee, Y. Zhu, and A. Seshia, “Sub- 10e charge resolution for room temperature electrometry,” *Proc. IEEE Sensors*, no. 1, pp. 821–824, 2007.

[6] J. E. Y. Lee, Y. Zhu, and A. A. Seshia, “A micromechanical electrometer approaching single-electron charge resolution at room temperature,” *Proc. IEEE Int. Conf. Micro Electro Mech. Syst.*, no. 1, pp. 948–951, 2008.

[7] P. S. Riehl, K. L. Scott, R. S. Muller, and R. T. Howe, “Capacitor,” *Circuit Des.*, pp. 305–308, 2002.

[8] J. Lee, Y. Zhu, A. Seshia, N. Centre, and U. Kingdom, “A variable capacitor based mems electrometer 1,” no. September 2006, 2017.

[9] G. Jaramillo, C. Buffa, M. Li, F. J. Brechtel, G. Langfelder, and D. A. Horsley, “MEMS electrometer with femtoampere resolution for aerosol particulate measurements,” *IEEE Sens. J.*, vol. 13, no. 8, pp. 2993–3000, 2013.

[10] Chunrong Peng, Xianxiang Chen, Qiang Bai, Lei Luo, and Shanhong Xia, “A Novel High Performance Micromechanical Resonant Electrostatic Field Sensor Used In Atmospheric Electric Field Detection,” *19th IEEE Int. Conf. Micro Electro Mech. Syst.*, no. January, pp. 698–701, 2006.

[11] X. Chen, C. Peng, and S. Xia, “Design of a Thermally Driven Resonant Miniature Electric Field Sensor with Feedback Control,” pp. 253–256, 2008.

[12] K. Bang Lee, *Principles of Microelectromechanical Systems*. 2011.

[13] R. I. Shakoor, “DESIGN , FABRICATION AND CHARACTERIZATION OF

METALMUMPs BASED MEMS GYROSCOPES," no. May, 2010.

[14] A. N. Cleland and M. L. Roukes, "A nanometre-scale mechanical electrometer," *Nature*, vol. 392, no. 6672, pp. 160–162, 1998.

[15] R. H. Blick, A. Erbe, H. Krömmer, A. Kraus, and J. P. Kotthaus, "Charge detection with nanomechanical resonators," *Phys. E Low-dimensional Syst. Nanostructures*, vol. 6, no. 1, pp. 821–827, 2000.

[16] J. S. Bunch *et al.*, "Electromechanical Resonators from Graphene Sheets," *Science (80-.).*, vol. 315, no. 5811, pp. 490–493, 2007.

[17] A. N. Cleland and M. L. Roukes, "Noise processes in nanomechanical resonators," *J. Appl. Phys.*, vol. 92, no. 5, pp. 2758–2769, 2002.

[18] J. E. Y. Lee, B. Bahreyni, and A. A. Seshia, "An axial strain modulated double-ended tuning fork electrometer," *Sensors Actuators, A Phys.*, vol. 148, no. 2, pp. 395–400, 2008.

[19] J. Zhao, H. Ding, and J. Xie, "Electrostatic charge sensor based on a micromachined resonator with dual micro-levers," *Appl. Phys. Lett.*, vol. 106, no. 23, p. 233505, 2015.

[20] J. Zhao, H. Ding, S. Ni, L. Fu, W. Wang, and J. Xie, "High-resolution and large dynamic range electrometer with adjustable sensitivity based on micro resonator and electrostatic actuator," in *2016 IEEE 29th International Conference on Micro Electro Mechanical Systems (MEMS)*, 2016, pp. 1074–1077.

[21] H. Zhang, J. Huang, W. Yuan, and H. Chang, "A High-Sensitivity Micromechanical Electrometer Based on Mode Localization of Two Degree-of-Freedom Weakly Coupled Resonators," *J. Microelectromechanical Syst.*, vol. 25, no. 5, pp. 937–946, Oct. 2016.

[22] Y. Zhu, J. E. Lee, S. Member, and A. a Seshia, "Charge Sensor," vol. 8, no. 9, pp. 1499–1505, 2008.

[23] D. P. Loconto and R. S. Muller, "High-sensitivity micromechanical electrostatic voltmeter," in *Proc. 7th Int. Conference on MEMS*, 1992.

[24] C. Peng, P. Yang, H. Zhang, X. Guo, and S. Xia, "Design of a novel closed-loop SOI MEMS resonant electrostatic field sensor," *Procedia Eng.*, vol. 5, pp. 1482–

1485, 2010.

[25] B. Ling *et al.*, “Design, fabrication and characterization of a MEMS-based three-dimensional electric field sensor with low cross-axis coupling interference,” *Sensors (Switzerland)*, vol. 18, no. 3, pp. 1–13, 2018.

[26] C. Science *et al.*, “A MEMS-Based , High-Resolution Electric-Field Meter John Sawa Shafran,” 2005.

[27] A. Kainz *et al.*, “Distortion-free measurement of electric field strength with a MEMS sensor,” *Nat. Electron.*, vol. 1, no. 1, pp. 68–73, 2018.

[28] A. Cowen, B. Hardy, R. Mahadevan, and S. Wilcenski, “PolyMUMPs Design Handbook, Rev. 13,” *Memscap*, 2013.

[29] R. Abdolvand, B. Bahreyni, J. E. Y. Lee, and F. Nabki, “Micromachined resonators: A review,” *Micromachines*, vol. 7, no. 9, 2016.

[30] G. Underwood, T. Laurvick, G. Underwood, and T. Laurvick, “MEMS Variable Area Capacitor for Room Temperature Electrometry,” *Proceedings*, vol. 2, no. 13, p. 1075, 2018.

[31] L. I. LIN, “A concordance correlation coefficient to evaluate reproducibility,” *Biometrics*, vol. 45, pp. 255–268, 1989.

[32] C. Peng *et al.*, “Design and testing of a micromechanical resonant electrostatic field sensor,” *J. Micromechanics Microengineering*, vol. 16, no. 5, pp. 914–919, 2006.

[33] H. Qu, “CMOS MEMS Fabrication Technologies and Devices,” *Micromachines*, vol. 7, no. 1, 2016.

REPORT DOCUMENTATION PAGE

Form Approved
OMB No. 074-0188

The public reporting burden for this collection of information is estimated to average 1 hour per response, including the time for reviewing instructions, searching existing data sources, gathering and maintaining the data needed, and completing and reviewing the collection of information. Send comments regarding this burden estimate or any other aspect of the collection of information, including suggestions for reducing this burden to Department of Defense, Washington Headquarters Services, Directorate for Information Operations and Reports (0704-0188), 1215 Jefferson Davis Highway, Suite 1204, Arlington, VA 22202-4302. Respondents should be aware that notwithstanding any other provision of law, no person shall be subject to an penalty for failing to comply with a collection of information if it does not display a currently valid OMB control number.
PLEASE DO NOT RETURN YOUR FORM TO THE ABOVE ADDRESS.

1. REPORT DATE *(DD-MM-YYYY)*	2. REPORT TYPE	3. DATES COVERED *(From – To)*
21-03-2019	Master’s Thesis	August 2017 – March 2019

TITLE AND SUBTITLE

A MEMS Dual Vertical Electrometer and Electric Field-Mill

5a. CONTRACT NUMBER

5b. GRANT NUMBER

5c. PROGRAM ELEMENT NUMBER

6. AUTHOR(S)

Underwood, George C., 2d Lt, USAF

5d. PROJECT NUMBER

5e. TASK NUMBER

5f. WORK UNIT NUMBER

7. PERFORMING ORGANIZATION NAMES(S) AND ADDRESS(S)

Air Force Institute of Technology
Graduate School of Engineering and Management (AFIT/EN)
2950 Hobson Way, Building 640
WPAFB OH 45433-8865

8. PERFORMING ORGANIZATION REPORT NUMBER

AFIT-ENG-19-M-063

9. SPONSORING/MONITORING AGENCY NAME(S) AND ADDRESS(ES)

Intentionally Left Blank

10. SPONSOR/MONITOR’S ACRONYM(S)

11. SPONSOR/MONITOR’S REPORT NUMBER(S)

12. DISTRIBUTION/AVAILABILITY STATEMENT

DISTRUBTION STATEMENT A. APPROVED FOR PUBLIC RELEASE; DISTRIBUTION UNLIMITED.

13. SUPPLEMENTARY NOTES

This material is declared a work of the U.S. Government and is not subject to copyright protection in the United States.

14. ABSTRACT

Presented is the first iteration of a Microelectromechanical System (MEMS) dual vertical electrometer and electrostatic field-mill (EFM) sensor. The device uses a resonating structure to create a variable capacitance that modulates a charge or field into an electrical signal. Previous MEMS electrometers are lateral electrometers with laterally spaced electrodes that resonate tangentially with respect to each other. Vertical electrometers, as the name suggests, have vertically spaced electrodes that resonate parallel with respect to each other. The non-tangential movement reduces damping in the system. Both types demonstrate comparable performance, but the vertical electrometer does so at a fraction of the size. In addition, the vertical electrometer can easily have an electric field sensor mode. The electric field sensor simulations did not compare as well to other MEMS electric field sensors. However, the duel nature of this device makes it appealing. These devices can be used in missiles and satellites to monitor charge buildup in electronic components and the atmosphere [11]. Future iterations can improve these devices and give way to inexpensive, high-resolution electrostatic charge and field sensors.

15. SUBJECT TERMS

MEMS electrometer, MEMS electric field-mill, electrometry

16. SECURITY CLASSIFICATION OF:			17. LIMITATION OF ABSTRACT	18. NUMBER OF PAGES	19a. NAME OF RESPONSIBLE PERSON
a. REPORT	b. ABSTRACT	c. THIS PAGE			Maj Tod Laurvick, AFIT/ENG
U	U	U	UU	104	19b. TELEPHONE NUMBER *(Include area code)* (937) 255-6565, ext 4382 (NOT DSN) (tod.laurvick@afit.edu)

Standard Form 298 (Rev. 8-98)
Prescribed by ANSI Std. Z39-18